

Higher-Rank Spin Liquids and Spin Nematics from Competing Orders in Pyrochlore Magnets

Niccolò Francini, Lukas Janssen, and Daniel Lozano-Gómez

Institut für Theoretische Physik and Würzburg-Dresden Cluster of Excellence ct.qmat, TU Dresden, 01062 Dresden, Germany

(Dated: September 5, 2024)

Pyrochlore magnets have proven to provide an excellent arena for the realization of a variety of many-body phenomena such as classical and quantum order-by-disorder, as well as spin liquid phases described by emergent gauge field theories. These phenomena arise from the competition between different symmetry-breaking magnetic orders. In this work, we consider a subspace of the most general bilinear nearest-neighbor Hamiltonian on the pyrochlore lattice, parameterized by the local interaction parameter $J_{z\pm}$, where three symmetry-breaking phases converge. We demonstrate that for small values of $|J_{z\pm}|$, a conventional $\mathbf{q} = 0$ ordered phase is selected by an thermal order-by-disorder mechanism. For $|J_{z\pm}|$ above a certain finite threshold, a novel spin-nematic phase is stabilized at low temperatures. Instead of the usual Bragg peaks, the spin-nematic phase features lines of high intensity in the spin structure factor. At intermediate temperatures above the low-temperature orders, a rank-2 U(1) classical spin liquid is realized for all $J_{z\pm} \neq 0$. We fully characterize all phases using classical Monte-Carlo simulations and a self-consistent Gaussian approximation.

I. INTRODUCTION

In the search for novel states of matter and associated exotic many-body phenomena, the study of frustrated magnets plays a pivotal role. Traditionally, magnetic frustration is categorized into two distinct classes. *Geometric frustration* occurs when the lattice geometry prevents spins from simultaneously satisfying all interaction constraints [1–3]. This phenomenon is commonly observed in lattices with corner-sharing triangular motifs, such as the Kagome [4] lattice in two dimensions and the pyrochlore [5] lattice in three dimensions. *Exchange frustration*, on the other hand, arises when the interactions between spins are inherently competing, independent of the lattice geometry. Recent research in this context has focused on magnets with highly anisotropic interactions, induced by significant spin-orbit coupling [6]. A particularly intriguing scenario arises when both geometric and exchange frustration mechanisms are simultaneously relevant. This situation can occur in pyrochlore compounds of the form $A_2M_2O_7$, where A and M are rare-earth and transition-metal elements, respectively [5]. The coexistence of both types of frustration can lead to the emergence of novel exotic phenomena that are absent when only one frustration mechanism is present.

The pyrochlore lattice, composed of a network of corner-sharing tetrahedra, provides an excellent platform for studying novel states of matter and associated many-body phenomena. This lattice has enabled significant research into spin liquids [7–16], order-by-disorder (ObD) phenomena [3, 17–23], magnetic fragmentation [24–26], and topological magnons [27]. Of particular interest is the realization of spin liquids, disordered yet strongly-correlated phases of matter, whose low-temperature behaviors are described by emergent gauge field theories [28]. In the case of classical spin liquids, these phases are characterized by an extensive ground state degeneracy, reflected in the occurrence of low-energy flat bands in the spectrum of the interaction matrix [28, 29]. These exotic phases of matter have turned out to be quite elusive and are usually associated with a delicate and balanced competition between different magnetic orders, preventing the formation of a symmetry-broken state at low temperatures. Recent work has illustrated how such delicate balance might

be realized at points in the interaction parameter space where multiple magnetic orders intersect [10, 14]. The stability of a spin liquid at these points may be however hampered by an ObD mechanism, whereas thermal or quantum fluctuations select a set of states out of the spin liquid’s extensively degenerate manifold resulting in a symmetry-breaking spin configuration. Indeed, previous studies [22] have demonstrated how such an ObD selection takes place at phase boundaries between distinct magnetic phases, typically resulting in a magnetically ordered $\mathbf{q} = 0$ phase at low temperatures.

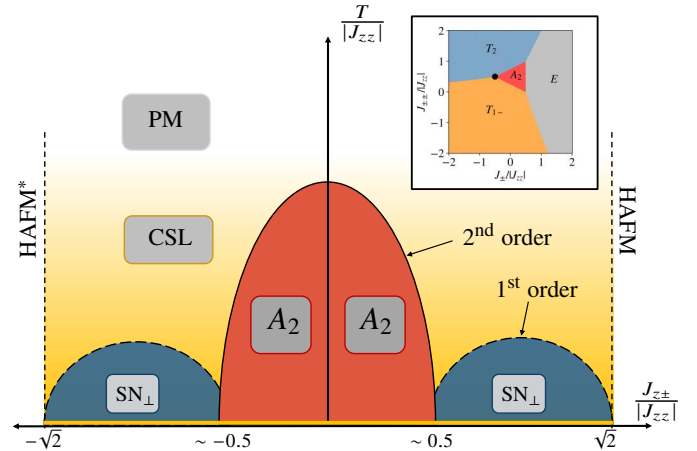


FIG. 1. Schematic finite-temperature phase diagram of the model in Eq. (1) as function of the coupling $J_{z\pm}$, with J_{\pm} and $J_{\pm\pm}$ tuned to the triple point between the A_2 , T_{1-} , and T_2 phases. As the temperature decreases, we observe a crossover from a high-temperature paramagnetic (PM) phase to an intermediate-temperature classical spin liquid (CSL), followed by a phase transition into one of two possible symmetry-broken states: a $\mathbf{q} = 0$ all-in-all-out antiferromagnet (A_2) or a non-magnetic spin nematic (SN_{\perp}) consisting of fluctuating components of the T_{1-} and T_2 irreps. Full (dashed) lines indicate continuous (discontinuous) phase transitions. The inset displays the zero-temperature phase diagram as a function of J_{\pm} and $J_{\pm\pm}$ for fixed $J_{z\pm} > 0$ and $J_{zz} < 0$ [5]. The black circle marks the triple phase boundary investigated in this work. At this point, the ground state is extensively degenerate, as highlighted by the thick yellow line at $T = 0$ in the main panel.

In this work, we present a detailed study of the distinct phases resulting from a thermal ObD selection for a model where three distinct long-range ordered phases intersect. We demonstrate that the strong competition between these phases results in a spin liquid regime at intermediate temperatures, characterized by twofold and fourfold pinch points in the spin structure factor. We show how the spin liquid phase is destabilized at low temperatures, resulting in a symmetry-breaking transition into a conventional $\mathbf{q} = 0$ magnetically ordered phase or a novel spin-nematic (SN_\perp) phase. We then show that the novel SN_\perp phase can be further stabilized at low temperatures across an extended region in parameter space, where only two distinct long-range ordered phases intersect.

We consider the bilinear nearest-neighbor Hamiltonian [5]

$$\mathcal{H} = \sum_{\langle ij \rangle} \left\{ J_{zz} S_i^z S_j^z - J_\pm (S_i^+ S_j^- + S_i^- S_j^+) + J_{\pm\pm} (\gamma_{ij} S_i^+ S_j^+ + \text{h.c.}) + J_{z\pm} (\zeta_{ij} S_i^z (S_j^+ + S_j^-) + \text{h.c.}) \right\}, \quad (1)$$

where S_i^z and $S_i^\pm = S_i^x \pm iS_i^y$ represent the components of the (pseudo) spin-1/2 on site i in a *local* coordinate frame, and the bond-dependent phase factors $\gamma_{ij} = -\zeta_{ij}^*$ are given in Appendix A of Ref. [30]. We first focus on a line in parameter space parameterized by the coupling $J_{z\pm}$, which we dub the $A_2 \oplus T_1 \oplus T_2$ line, where two antiferromagnetic phases A_2 [31] and T_2 [32] and a ferromagnetic phase T_{1-} [33] intersect. The competition between these three phases results in an extensively-degenerated ground state manifold which, at intermediate temperatures, leads to a rank-1 U(1) spin liquid phase for $J_{z\pm} = 0$ and a rank-2 U(1) spin liquid for $J_{z\pm} \neq 0$. At low temperatures, the spin liquid phases are destabilized by symmetry-breaking ObD selection to a $\mathbf{q} = 0$ state for $|J_{z\pm}|/|J_{zz}| \lesssim 0.5$ and to a spin-nematic phase for $0.5 \lesssim |J_{z\pm}|/|J_{zz}| < \sqrt{2}$. Our results are summarized in the schematic phase diagram shown in Fig. 1. We then demonstrate that the same qualitative low-temperature physics resulting on a spin nematic state are observed along the $A_2 \oplus T_1 \oplus T_2$ line for $0.5 \lesssim |J_{z\pm}|/|J_{zz}| < \sqrt{2}$ can also be found across an entire plane in parameter space, parameterized by $J_{z\pm}$ and J_\pm . This plane, referred to as the $T_1 \oplus T_2$ plane, is where the ferromagnetic phase T_{1-} intersects with only one of the antiferromagnetic phases, namely T_2 .

The remainder of the paper is organized as follows: In Sec. II, we introduce the irreducible representations of the single-tetrahedron Hamiltonian and provide the parametrization describing the $A_2 \oplus T_1 \oplus T_2$ line. In Sec. III, we briefly introduce the self-consistent Gaussian approximation and present the low-energy bands of the models parametrized by the $A_2 \oplus T_1 \oplus T_2$ line. Section IV contains details of our Monte-Carlo approach and a list of thermodynamics quantities measured in the classical simulations. A detailed analysis for $J_{z\pm} = 0$, i.e., the non-Kramers Hamiltonian, for which a rank-1 spin liquid phase is realized at intermediate temperatures, is provided in Sec. V. In Sec. VI, we consider the case $|J_{z\pm}| > 0$, for which a rank-2 U(1) spin liquid is realized at intermediate temperatures. In this section, we also discuss in detail the two distinct parameter regimes where $\mathbf{q} = 0$ and SN_\perp phases,

respectively, are selected at low temperatures. We conclude in Sec. VII. Technical details are deferred to four appendices.

II. IRREDUCIBLE REPRESENTATION ANALYSIS

In this section, we present an overview of the irreducible representation analysis conducted for a generic nearest-neighbor dipolar Hamiltonian on the pyrochlore lattice. In the classical limit, and exploiting the corner-sharing geometry of the pyrochlore lattice, the Hamiltonian in Eq. (1) can be written as

$$\mathcal{H} = \sum_{\boxtimes} \mathcal{H}_{\boxtimes}, \quad (2)$$

where \sum_{\boxtimes} denotes the sum over all tetrahedra and \mathcal{H}_{\boxtimes} represents the single-tetrahedron Hamiltonian. This single-tetrahedron Hamiltonian can be expressed in terms of irreducible representations (irreps) [34],

$$\mathcal{H}_{\boxtimes} = a_{A_2} \mathbf{m}_{A_2}^2 + a_E \mathbf{m}_E^2 + a_{T_2} \mathbf{m}_{T_2}^2 + a_{T_{1-}} \mathbf{m}_{T_{1-}}^2 + a_{T_{1+}} \mathbf{m}_{T_{1+}}^2, \quad (3)$$

where the A_2 , E , T_2 , T_{1-} , and T_{1+} label the spin modes describing the all-in-all-out (AIAO) [25, 31], Γ_5 [19, 35, 36], Palmer-Chalker [32, 37], and two types of splayed ferromagnetic orders [30, 33],¹ respectively. \mathbf{m}_I is the spin mode in a single tetrahedron corresponding to the I th irrep, and a_I is a function of the interaction parameters $\{J_{zz}, J_\pm, J_{\pm\pm}, J_{z\pm}\}$ representing the internal energy cost associated with the I th irrep. For more details regarding the explicit form of the \mathbf{m}_I spin modes and their corresponding single-tetrahedron energies a_I we refer to Appendix A.

Recent work [34, 38] has demonstrated the utility of the above irrep decomposition for generating ground state phase diagrams. In particular, this approach allows one to identify the irreps with the minimum energy cost a_I , and aids in predicting effective gauge theories describing spin liquid phases in cases when multiple irreducible representations are energetically degenerate and no symmetry-breaking transition occurs [28]. In the context of the present work, we study the different phases accessed as a function of temperature when the A_2 , T_{1-} , and the T_2 irreps compete, and the two remaining irreps (namely the E and the T_{1+} irreps) are gapped at higher energies. In terms of the interaction parameters in Eq. (1), the region in parameter space where the A_2 , T_{1-} , and T_2 irreps are degenerate is defined by the parametrization

$$J_\pm = -\frac{J_{z\pm}^2}{J_{zz}} + \frac{3}{2}J_{zz} \quad \text{and} \quad J_{\pm\pm} = -\frac{J_{z\pm}^2}{2J_{zz}} \quad (4)$$

with the constraints

$$J_{zz} < 0 \quad \text{and} \quad |J_{z\pm}| < \sqrt{2}|J_{zz}|. \quad (5)$$

¹ There are special cases for which the two T_1 irreps represent a colinear ferromagnet and a coplanar antiferromagnet.

The above functional form of the interaction parameters identifies a line in the interaction parameter space as a function of the coupling $J_{z\pm}$, which we refer to as the $A_2 \oplus T_1 \oplus T_2$ line. The boundaries of this line are the points $J_{z\pm} = \pm\sqrt{2}|J_{zz}|$, which correspond to two spin liquid points, the Heisenberg antiferromagnet for $J_{z\pm} > 0$ and its dual for $J_{z\pm} < 0$ [39]. Furthermore, this parametrization can be segmented in two families of Hamiltonians: the non-Kramers Hamiltonian for which $J_{z\pm} = 0$, and the Kramers Hamiltonian for which $J_{z\pm} \neq 0$ [5].

In what follows, we map out the finite-temperature phase diagram as function of $J_{z\pm}$ along the $A_2 \oplus T_1 \oplus T_2$ line, first focusing on the non-Kramers Hamiltonian in Sec. V, and then proceeding to the Kramers Hamiltonian in Sec. VI. The $A_2 \oplus T_1 \oplus T_2$ line is a subset of the $T_1 \oplus T_2$ plane. As a consequence, a complete characterization of this subset will facilitate a comprehensive understanding of the entire $T_1 \oplus T_2$ plane, which will be detailed towards the end of Sec. VI. Before continuing, we note that the model in Eq. (1) features a duality under changing the sign of $J_{z\pm}$ followed by a $\pi/2$ rotation about the local z axis of all spin [5]. Consequently, for the Kramers Hamiltonian, we only present results for the case for which $J_{z\pm} \geq 0$, and extend our results to the $J_{z\pm} < 0$ case using the duality relation. From this point on, and based on the parametrization of the $A_2 \oplus T_1 \oplus T_2$ line, we assume units in which the Boltzmann constant $k_B = 1$ and measure all energies in units of $|J_{zz}| = 1$.

III. SELF-CONSISTENT GAUSSIAN APPROXIMATION

The self-consistent Gaussian approximation (SCGA) [29, 40, 41] is a classical method in which the hard spin length constraint, $\mathbf{S}_i^2 = S^2$, is replaced by a soft constraint, $\sum_i \mathbf{S}_i^2 = NS^2$, where N corresponds to the total number of sites on the lattice. The latter can be easily implemented by the cost of a single Lagrange multiplier λ . This approximation yields a quadratic Hamiltonian that can be solved exactly, and from which the spin correlation functions and effective low-temperature theories can be studied. The starting point of this analysis is to rewrite the Hamiltonian in Eq. (1) as

$$\mathcal{H} = \frac{1}{2} \sum_{i,j} \mathbf{S}_i^T \mathbf{M}_{ij} \mathbf{S}_j, \quad (6)$$

where \mathbf{M}_{ij} denotes the 3×3 real-space interaction matrix for given fixed lattice sites i and j . In the SCGA, we have direct access to the static spin structure factor, given as

$$S(\mathbf{q}) = \sum_{\mu,\nu} \sum_{\alpha} \sum_{\mathbf{q}} (\beta \mathbf{M}_{\mu\nu}^{\alpha\alpha}(\mathbf{q}) + \lambda)^{-1}, \quad (7)$$

where β is the inverse temperature, $\mathbf{M}(\mathbf{q})$ is the 12×12 interaction matrix in reciprocal space, α labels the Cartesian spin components, and μ and ν label the sublattice structure. Note that the spin structure factor involves taking a trace with respect to the spin components, so Eq. (7) includes only the diagonal spin components of the interaction matrix.

For the $A_2 \oplus T_1 \oplus T_2$ line, the diagonalization of the interaction matrix $\mathbf{M}(\mathbf{q})$ results in the identification of four low-energy flat

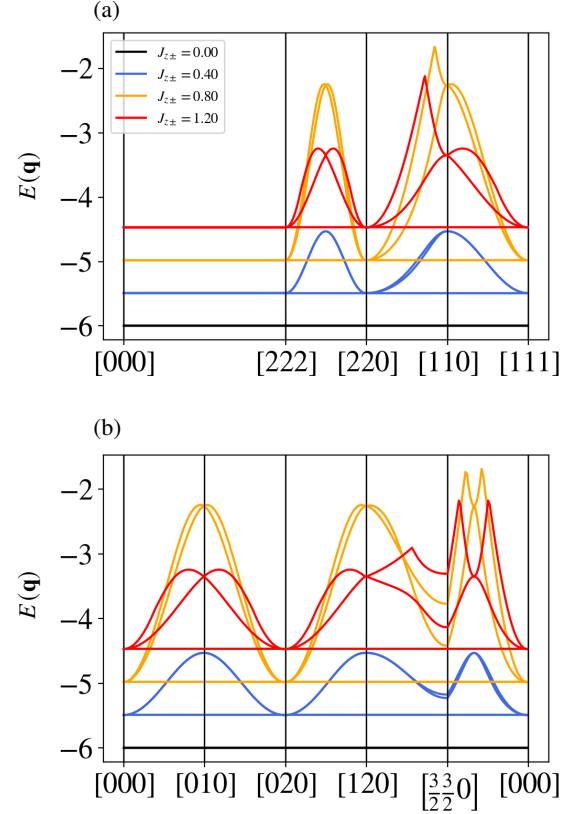


FIG. 2. Four lowest-energy bands in the spectrum of the interaction matrix \mathbf{M}_{ij} for different fixed values of $J_{z\pm}$ on the $A_2 \oplus T_1 \oplus T_2$ line, i.e., for J_{\pm} and $J_{\pm\pm}$ chosen according to Eq. (4), along high-symmetry paths in (a) the $[hhh]$ plane and (b) the $[hk0]$ plane in reciprocal space. Different colors indicate different values of $J_{z\pm}$, given in the inset of panel (a). For better visibility, different-colored bands have been offset by a constant energy shift of 0.5 from black to red.

bands for $J_{z\pm} = 0$ and two low-energy flat-bands for $J_{z\pm} \neq 0$, see Fig. 2. At the level of the SCGA, the observation of low-energy flat bands in the spectrum of the interaction matrix indicates the realization of a stable spin liquid phase down to the lowest temperatures [14, 40]. The SCGA, however, does not account for higher-order terms in a free-energy expansion, which may result in the ObD selection of a symmetry-breaking phase at low temperatures. Consequently, in order to assess the validity of the approximation, complementary methods must be used to determine the ultimate fate of the systems in the zero-temperature limit.

IV. CLASSICAL MONTE-CARLO SIMULATIONS

A. Algorithmic details

As an unbiased complementary method, we study the model in Eq. (1) using large-scale Monte-Carlo simulations based on the Metropolis and overrelaxation algorithm, equipped with

parallel tempering exchange. In the simulations, the spins are treated as classical vectors of unit length $\mathbf{S}_i^2 = 1$. For each lattice sweep of a Metropolis update, we combine 20 overrelaxation steps and propose a replica exchange of the configurations at adjacent temperatures. The procedure is repeated 20 times between two consecutive measurements on the lattice. We consider pyrochlore lattices with L^3 tetrahedra and $N = 4L^3$ sites, using $L = 8, 10, 12$ and employing periodic boundary conditions. The accumulated statistics is of the order $\mathcal{O}(10^5)$ for each point in parameter space [42].

B. Observables

In our simulations, we measure the following thermodynamic observables:

a. Energy density. The internal energy density ε is defined by the energy per site,

$$\varepsilon := \frac{\langle \mathcal{H} \rangle}{N}, \quad (8)$$

where N corresponds to the total number of sites.

b. Specific heat. From the fluctuations of the energy, we measure the specific heat as

$$C := \frac{\langle \mathcal{H}^2 \rangle - \langle \mathcal{H} \rangle^2}{NT^2}, \quad (9)$$

where T is the absolute temperature. Alternatively, the specific heat can be computed from the energy density as $C = \partial \varepsilon / \partial T$.

c. Magnetic order parameters. Magnetic order parameters can be formulated using the single-tetrahedron irreps \mathbf{m}_I , $I = A_2, E, T_2, T_{1\pm}$ as

$$\mathbf{m}_I = \left\langle \left| \frac{1}{L^3} \sum_{\boxtimes} \mathbf{m}_I \right| \right\rangle, \quad (10)$$

where \sum_{\boxtimes} denotes the sum over all tetrahedra on the lattice. The single-tetrahedron irreps \mathbf{m}_I are given explicitly in terms of the spins in Appendix A.

d. Spin-nematic order parameter. The single-site spin-nematic order parameter is defined as [10, 43–45]

$$Q_{\perp}^{\text{site}} = \left\langle \left| \frac{1}{N} \sum_i \begin{pmatrix} (S_i^x)^2 - (S_i^y)^2 \\ 2S_i^x S_i^y \end{pmatrix} \right| \right\rangle, \quad (11)$$

and is sensitive to the local xy arrangement of the spins.

e. Static spin structure factor. We also measure the static spin structure factor defined as

$$S(\mathbf{q}) = \frac{1}{N} \sum_{i,j} \langle \mathbf{S}_i \cdot \mathbf{S}_j \rangle e^{-i\mathbf{q} \cdot (\mathbf{R}_i - \mathbf{R}_j)}, \quad (12)$$

where \mathbf{R}_i is the position vector of the site i on the lattice. The spin structure factor allows for a direct comparison between our Monte-Carlo results and SCGA predictions. Moreover, in a spin liquid phase, it clearly reflects the properties of the

underlying emergent gauge field theory. Therefore, in the main text, we focus on the spin structure factor rather than neutron structure factors, which are more directly accessible experimentally. Results for the neutron structure factors at representative points along the $A_2 \oplus T_1 \oplus T_2$ line are presented in Appendix D.

V. NON-KRAMERS CASE $J_{z\pm} = 0$

We begin our analysis of the $A_2 \oplus T_1 \oplus T_2$ line by first considering the point along this line at which $J_{z\pm} = 0$. This scenario results in a non-Kramers Hamiltonian, with the local z spin degrees of freedom transforming as magnetic dipoles and the local xy degrees of freedom transforming as magnetic quadrupoles [5, 46]. In terms of irreps, the decoupling between the local z and local xy degrees of freedom is evident in the specific form of the T_1 irreps. These irreps correspond to two distinct splayed ferromagnetic configurations, where spins are either aligned along their local z axis or confined to their local xy plane [5, 10]. For the case $J_{z\pm} = 0$ in the parametrization of the $A_2 \oplus T_1 \oplus T_2$ line, the T_{1-} corresponds to local- xy splayed ferromagnet.

A. SCGA results

As was previously stated, the observation of four low-energy flat bands in the spectrum of the interaction matrix would imply that, at the level of SCGA, a spin liquid phase is realized. Following the identification of the low-energy flat bands, we use the irrep fields, as defined in Appendix A, and the effective Hamiltonian obtained through an SCGA analysis to obtain an effective model describing the low-energy physics. This procedure is fully analogous to those performed in recent studies [8, 11, 16], and we refer the reader to these works for further details. The spin liquid phase predicted by the SCGA analysis results in the identification of two rank-1 gauge fields, namely

$$\mathbf{E}^A = (2m_{T_{1-}}^x, -m_{T_{1-}}^y, -\sqrt{3}m_{T_2}^y, -m_{T_{1-}}^z + \sqrt{3}m_{T_2}^z), \quad (13)$$

$$\mathbf{E}^B = (2m_{T_2}^x, +\sqrt{3}m_{T_{1-}}^y - m_{T_2}^y, -\sqrt{3}m_{T_{1-}}^z - m_{T_2}^z), \quad (14)$$

which fulfill energetically-imposed Gauss's law at low temperatures

$$\partial_i E_i^A = 0 \quad \text{and} \quad \partial_i E_i^B = 0, \quad (15)$$

where we have assumed summation over repeated indices. In the above expressions, the m_I^α labels the α component of the I th irrep mode. The energetically-enforced Gauss's laws result in the observation of sharp twofold pinch features in the SCGA spin structure factor, see Fig. 3(a). We note that the gauge fields defined in Eqs. (13) and (14) do not have any component of the A_2 irrep. The absence of this contribution at low temperatures is due to the A_2 field adhering to its own Gauss's law, specifically $\partial_i m_{A_2} = 0$ [39, 47]. Given that the m_{A_2} is a one-dimensional field, the Gauss's law implies that

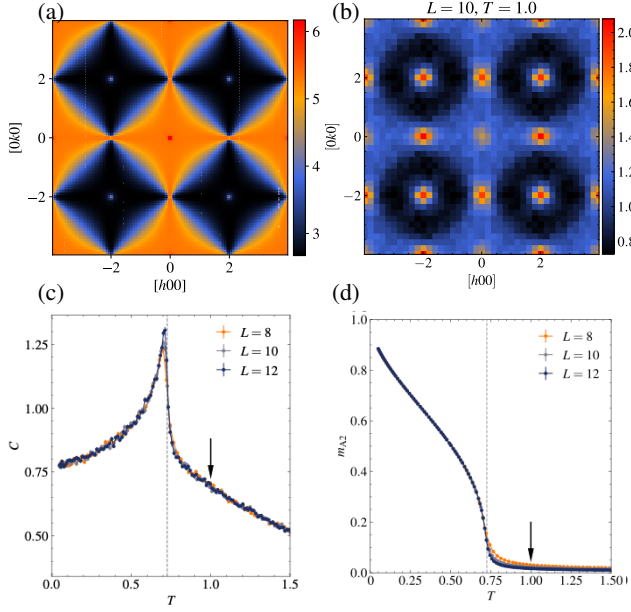


FIG. 3. (a) Static spin structure factor in the $[hk0]$ plane from SCGA in the low-temperature limit for the non-Kramers case $J_{z\pm} = 0$, describing the correlations in the rank-1 classical spin liquid. (b) Same as (a), but from classical Monte-Carlo simulations on an $L = 10$ lattice for a fixed temperature $T = 1$ above T_c . (c) Specific heat as function of temperature T for different lattice sizes, revealing a continuous transition in the 3D Ising universality class at $T_c = 0.7266(3)$. (d) Same as (c), but for the A_2 order parameter m_{A_2} . Dashed lines in (c) and (d) indicate the critical temperature. Arrows indicate the temperature chosen in (b).

at low temperatures, it can only obtain a uniform constant value throughout the lattice. In the absence of long-range order, the fulfilment of this Gauss's law would imply that $m_{A_2} = 0$. The effective gauge theory describing the spin liquid regime encompasses a total of six degrees of freedom, corresponding to the six components of the T_{1-} and T_2 irreps, associated with the gauge fields \mathbf{E}^A and \mathbf{E}^B . These are subject to two constraints provided by their respective Gauss's laws. Consequently, this framework identifies four flat bands for the $J_{z\pm} = 0$ spin liquid, resulting from the subtraction of the number of constraints from the total degrees of freedom, in agreement with the results shown in Fig. 2.

B. Classical Monte-Carlo results

To assess the stability of the spin liquid phase predicted by the SCGA analysis, we compare its predictions with the results obtained from classical Monte-Carlo simulations. For not too low temperatures, both approaches yield consistent results. In particular, at intermediate temperatures around $T \sim |J_{zz}| = 1$, the system effectively behaves as the classical spin liquid predicted by SCGA. The spin structure factors at $T = 1$, see Fig. 3(b), resemble the SCGA prediction modulo thermal broadening of the pinch points, where the broadening

of these features is associated with a non-zero population of gauge charges and therefore the violation of the Gauss's laws in Eq. (15). In the low-temperature limit, the classical spin liquid regime is not stable: the system eventually reaches a critical temperature T_c , below which a long-range $\mathbf{q} = 0$ order develops due to a thermal ObD mechanism, which we discuss in further detail below. At the transition, the specific heat shows a pronounced peak, as seen in Fig. 3(c). Among the three competing long-range ordered phases at the $A_2 \oplus T_1 \oplus T_2$ point, only one is selected, namely, the A_2 phase, as suggested by the corresponding magnetic order parameter m_{A_2} , shown in Fig. 3(d). Moreover, we have explicitly verified that the spin structure factor develops the Bragg-peak pattern expected for A_2 order (not shown) [31]. The AIAO state spontaneously breaks time reversal symmetry, suggesting that the transition, if continuous, belongs to the 3D Ising universality class. Indeed, through a standard finite-size scaling analysis of the Binder cumulant associated with m_{A_2} (not shown), we find the correlation-length exponent $\nu = 0.636(5)$, which is consistent with a continuous 3D Ising transition.

The thermal ObD selection can be understood using classical low-temperature expansion, which yields an effective quadratic Hamiltonian for the spin fluctuations about a ground-state configuration [22]. Through this expansion, we identify the spin configuration with the lowest energy fluctuations, which is then expected to be thermally selected at low temperatures [34]. For a $\mathbf{q} = 0$ state, this expansion identifies 8 modes in reciprocal space. We study the energy fluctuations about the three competing $\mathbf{q} = 0$ magnetic orders along the $A_2 \oplus T_1 \oplus T_2$ line, where these three magnetic long-range orders compete. The effective Hamiltonian obtained for fluctuations about the T_{1-} and the T_2 states yields 8 quadratic dispersive bands. In contrast, for the A_2 state, this expansion identifies four zero-energy flat bands and four dispersive high-energy bands. As a consequence, the A_2 state is equipped with quadratic and at-least-quartic modes, resulting in lower energy fluctuations and a higher associated entropic weight [22]. The classical low-temperature expansion therefore suggests that the thermal ObD generates an entropic selection of the A_2 ground state. For more details on the expansion, we refer to Appendix B.

The quadratic and at-least-quartic modes about the A_2 state leave a signature in the low-temperature value of the specific heat. In particular, if we assume that the zero-energy fluctuation modes in the classical low-temperature expansion are quartic, from the equipartition theorem, the specific heat in units of k_B in the limit of low temperature follows,

$$C = \frac{1}{4} \left(\frac{n_2}{2} + \frac{n_4}{4} \right), \quad (16)$$

where n_2 and n_4 are the numbers of quadratic and quartic modes, respectively, with $n_2 + n_4 = 8$ being the total number of modes. For the A_2 state, we then have $n_2 = n_4 = 4$, from which we obtain the prediction $C = 3/4$ for the specific heat at zero temperature, which agrees with the numerical results shown in Fig. 3(c), confirming that the zero-energy modes in the effective quadratic theory are quartic modes.

VI. KRAMERS CASE $J_{z\pm} \neq 0$

A. SCGA results

We now discuss the Kramers case for which $J_{z\pm} \neq 0$. As for the non-Kramers case, we first start by providing an SCGA analysis and then supplement this with a classical Monte-Carlo study. Similarly to the $J_{z\pm} = 0$ case, the Hamiltonian describing the $A_2 \oplus T_1 \oplus T_2$ line for $J_{z\pm} \neq 0$ presents flat bands in the interaction matrix spectrum. In this case however, the number of flat bands reduces to two out of twelve. Nevertheless, in an SCGA analysis, the observation of low-energy flat bands implies the realization of a spin liquid phase. In this case however, the system is described by three emergent gauge fields, of which two are rank-1 gauge fields, namely

$$\begin{aligned} \mathbf{E}^{A_{z\pm}} = & (2 \sin \phi m_{T_{1-}}^x, -\sin \phi m_{T_{1-}}^y - \sqrt{3} m_{T_2}^y, \\ & -\sin \phi m_{T_{1-}}^z + \sqrt{3} m_{T_2}^z), \end{aligned} \quad (17)$$

$$\begin{aligned} \mathbf{E}^{B_{z\pm}} = & (2 m_{T_2}^x, +\sqrt{3} \sin \phi m_{T_{1-}}^y - m_{T_2}^y, \\ & -\sqrt{3} \sin \phi m_{T_{1-}}^z - m_{T_2}^z), \end{aligned} \quad (18)$$

and the remaining gauge field is a rank-2 field,

$$\begin{aligned} \mathbb{E}^{A_2+T_1+T_2} = & -\sin \phi \begin{bmatrix} m_{A_2} & 0 & 0 \\ 0 & m_{A_2} & 0 \\ 0 & 0 & m_{A_2} \end{bmatrix} \\ & + \frac{\cos \phi}{2} \begin{bmatrix} 0 & \sqrt{3} m_{T_2}^z & -\sqrt{3} m_{T_2}^y \\ -\sqrt{3} m_{T_2}^z & 0 & \sqrt{3} m_{T_2}^x \\ \sqrt{3} m_{T_2}^y & -\sqrt{3} m_{T_2}^x & 0 \end{bmatrix} \\ & + 2 \sin \phi \cos \phi \begin{bmatrix} 0 & m_{T_{1-}}^z & m_{T_{1-}}^y \\ m_{T_{1-}}^z & 0 & m_{T_{1-}}^x \\ m_{T_{1-}}^y & m_{T_{1-}}^x & 0 \end{bmatrix}, \end{aligned} \quad (19)$$

where the angle ϕ corresponds to the decoupling angle between the two T_1 irreps, see Appendix A. At low energies, these fields are constraint by three energetically-imposed Gauss's law constraints

$$\begin{aligned} \partial_i E_i^{A_{z\pm}} &= 0, \\ \partial_i E_i^{B_{z\pm}} &= 0, \\ \partial_i \mathbb{E}_{ij}^{A_2+T_1+T_2} &= 0. \end{aligned} \quad (20)$$

Note that the construction of the rank-2 tensor $\mathbb{E}^{A_2+T_1+T_2}$ includes irrep fields that also appear in the construction of the rank-1 fields, $\mathbf{E}^{A_{z\pm}}$ and $\mathbf{E}^{B_{z\pm}}$. Consequently, the Gauss's law constraints on the rank-1 fields can be seen as additional constraints on the rank-2 field. According to the Gauss's law constraints in Eq. (20) for the rank-2 field, the system realizes a rank-2 U(1) spin liquid characterized by fourfold pinch points in the spin structure factor [48]. The observation of these fourfold features is associated with the realization of fractons, excitations whose diffusion is severely restricted by the presence of charge, dipole, and possibly other multipole conservation laws [48–50]. We emphasize that the observation

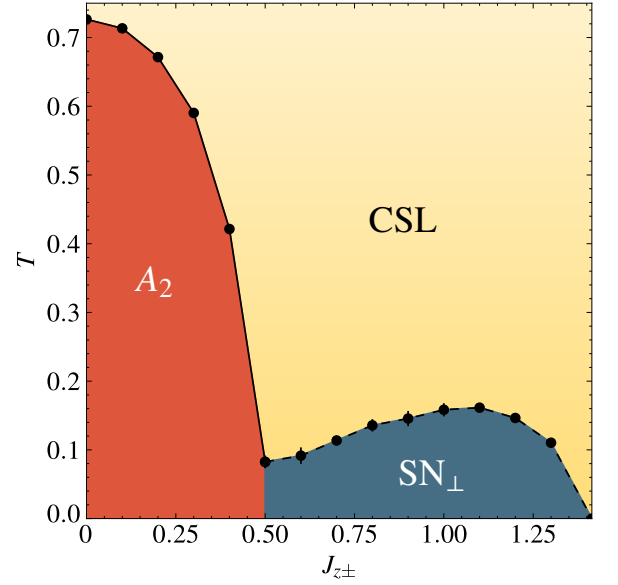


FIG. 4. Finite-temperature phase diagram of the $A_2 \oplus T_1 \oplus T_2$ line from classical Monte-Carlo simulations. The classical spin liquid (CSL) at intermediate temperatures (yellow region) features thermally broadened four-fold pinch points in the spin structure factor, associated with the emergence of a rank-2 U(1) gauge field. For $J_{z\pm} < 0.5$, the model exhibits a continuous ordering transition towards a $\mathbf{q} = 0$ AIAO antiferromagnet (A_2) at low temperatures (red region). For $J_{z\pm} > 0.5$, a first-order finite-temperature transition towards a nonmagnetic spin nematic (SN_{\perp}) is realized (blue region). The spin nematic is characterized by continuous intensity lines in the spin structure factor and three macroscopically-degenerate sets of ground states. Each set is composed of two fluctuating components of T_{1-} and T_2 irreps, with the respective third component being suppressed in each case.

of fourfold pinch points, either broad or sharp, is expected for all non-vanishing $J_{z\pm}$ on the $A_2 \oplus T_1 \oplus T_2$ line, as the general structure of the Gauss's laws and fields remains unchanged at the level of the SCGA. The higher-rank spin liquid observed for $J_{z\pm} \neq 0$ is characterized by seven degrees of freedom, corresponding to the seven fluctuating fields (the components of the A_2 , T_{1-} , and T_2 fields), and five constraints provided by the two scalar and three vector components of the Gauss's laws in Eq. (20). As a result, this spin liquid is characterized by two low-energy flat bands, in agreement with the results shown in Fig. 2.

B. Classical Monte-Carlo results

We now assess the validity of the SCGA predictions using the classical Monte-Carlo approach. For all values of $J_{z\pm} \in (0, \sqrt{2})$ and not too low temperatures, we find both approaches to yield consistent results, as in the non-Kramers case for $J_{z\pm} = 0$ discussed above. In particular, the spin structure factor measured in the Monte-Carlo simulations is consistent with the emergence of a classical higher-rank spin liquid regime at intermediate temperatures. At low temperatures, we observe a finite-temperature transition towards to one out of two possible

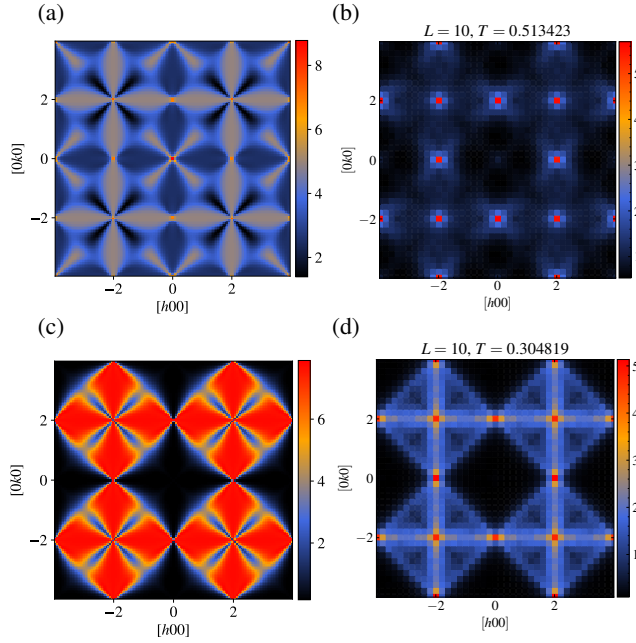


FIG. 5. (a) Static spin structure factor in the $[hk0]$ plane from SCGA in the low-temperature limit for the Kramers case, using a representative value of $J_{z\pm} = 0.4$, describing the correlations in the rank-2 classical spin liquid. (b) Same as (a), but from classical Monte-Carlo simulations on an $L = 10$ lattice for a fixed temperature $T = 0.51$ above T_c . (c) Same as (a), but for a value of $J_{z\pm} = 1$. (d) Same as (c), but from classical Monte-Carlo simulations on an $L = 10$ lattice for a fixed temperature $T = 0.30$ above T_c . We note that in all panels fourfold pinch points, or remnants of such correlations, can be observed at the $[220]$ and symmetry related points.

symmetry-broken states: a $\mathbf{q} = 0$ AIAO antiferromagnet for $J_{z\pm} < 0.5$ and a non-magnetic spin nematic for $J_{z\pm} > 0.5$, see Fig. 4. In the following, we characterize the three states in detail.

1. Classical spin liquid

The SCGA analysis predicts a rank-2 $U(1)$ spin liquid phase for $|J_{z\pm}| > 0$. Figure 5(a) shows the corresponding spin structure factor from SCGA for a representative value of $J_{z\pm} = 0.4$, indicating the emergence of fourfold (twofold) pinch points at $[220]$ ($[020]$) and symmetry-related points in the $[hk0]$ plane in reciprocal space. These features can be understood to descend from the Gauss' laws in Eq. (20). For intermediate temperatures, our large-scale Monte-Carlo simulations reveal broadened versions of the combined twofold and fourfold pinch-point pattern. The intermediate-temperature regime can thus be understood as an excited state of the higher-rank spin liquid found in SCGA, where gauge charges are present and the higher-rank Gauss's law is violated. This is illustrated in Fig. 5(b), which shows the static spin structure factor for $J_{z\pm} = 0.4$ at a fixed finite temperature slightly above the transition temperature.

The rank-2 spin liquid phase at intermediate temperatures

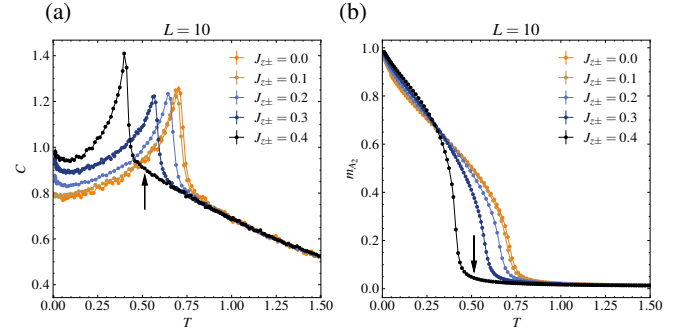


FIG. 6. (a) Specific heat as function of temperature T from classical Monte-Carlo simulations on an $L = 10$ lattice for different values of $J_{z\pm}$, indicating that T_c initially decreases with increasing $J_{z\pm}$. (b) Same as (a), but for the A_2 order parameter m_{A_2} . Arrows in (a) and (b) indicate the temperatures chosen for the spin structure factor measured in Fig. 5(b).

predicted by the SCGA analysis can be understood as a single phase for $J_{z\pm} > 0$, this however does not imply that all the thermodynamic signatures in this phase remain unchanged as a function of the interaction parameter $J_{z\pm}$. Indeed, the Gauss's laws in Eq. (20) possess an implicit dependence on the $J_{z\pm}$ parameter encoded in the T_{1-} field, see Appendix A. This functional dependence is reflected in the spin structure factors of the corresponding model. Figures 5(a) and 5(c) show the SCGA predictions for the spin structure factor for $J_{z\pm} = 0.4$ and $J_{z\pm} = 1$, respectively, both possessing twofold and fourfold pinch points. A similar evolution in the static spin structure factor is observed in the classical Monte-Carlo simulations, as shown in Figs. 5(b) and 5(d), for the same set of interaction parameters, but at a fixed finite temperature slightly above the transition temperature. Indeed, the qualitative agreement between Figs. 5(b) and 5(d) and their corresponding SCGA predictions indicates that the spin-liquid regime persists above the low-temperature order throughout the phase diagram.

2. A_2 all-in-all-out antiferromagnet

Similarly to the non-Kramers case, we assess the low-temperature fate of the classical spin liquid using the Monte-Carlo approach. For $J_{z\pm} < 0.5$, the low-temperature behavior in the Kramers case resembles that of the non-Kramers case $J_{z\pm} = 0$, where a continuous transition into a long-range ordered phase is observed, see Fig. 6(a), into a $\mathbf{q} = 0$ AIAO antiferromagnetic order characterized the A_2 irrep, see Fig. 6(b). We note that the precise T_c depends on $J_{z\pm}$, see Fig. 6(a).

For finite $J_{z\pm} \in (0, 0.5)$, the behavior of the system within the A_2 ordered phase is quite remarkable. As shown in Fig. 6(a), for decreasing temperature T , the specific heat initially decreases below one and eventually increases again toward one at extremely low temperatures. We note that the upturn in the specific heat below T_c becomes more prominent for larger $J_{z\pm}$. This behavior can be understood in terms of the classical low-temperature expansion: for $J_{z\pm} > 0$, the four bands that are flat at quadratic order for the A_2 state in the non-Kramers case become dispersive, resulting in $n_2 = 8$

and $n_4 = 0$ in Eq. (16), leading to a specific heat of $C = 1$ in the low-temperature limit. For small but finite $J_{z\pm}$, however, the low-energy quadratic modes have a small band width. Thus, for temperatures larger than the band width of the low-energy quadratic modes, the low-energy fluctuations effectively emerge from a flat band, therefore decreasing the value of the specific heat. On the other hand, as the temperature is further decreased, the weak dispersions of the low-energy bands eventually become relevant, driving the system to a unit specific heat in the low-temperature limit, in agreement with the equipartition theorem of quadratic modes. As the width of the low-energy dispersive bands increases with $J_{z\pm}$, the characteristic temperature of the upturn should be expected to increase as well, in agreement with the trend observed in Fig. 6(a), and further shown in Appendix C. A more detailed analysis of the upturn in the specific heat may be obtained by extending the low-temperature expansion beyond the quadratic order. This is left for future work.

3. Spin nematic

As shown in Fig. 4, along the $A_2 \oplus T_1 \oplus T_2$ line, an ObD mechanism lifts the classical spin liquid degeneracy at low temperatures, driving the system into a symmetry-breaking low-temperature phase. As shown in the previous subsection, for $J_{z\pm} < 0.5$, the low-temperature symmetry-broken phase is a $\mathbf{q} = 0$ AIAO phase. Remarkably, for $J_{z\pm} > 0.5$, the nature of the low-temperature state changes abruptly. At low temperatures, the system realizes a novel spin nematic ground state, which lacks any magnetic long-range order. This is illustrated in Fig. 7(a), which shows the static spin structure factor from classical Monte-Carlo simulations for a representative value of $J_{z\pm} = 1$ and a fixed temperature below the transition temperature. The structure factor is characterized by the absence of any magnetic Bragg peaks and instead shows continuous intensity lines along $[2k0]$ and symmetry-related lines in the $[hk0]$ plane, which persist down to the lowest temperatures. Moreover, we have explicitly verified that all magnetic order parameters m_I , with $I \in \{A_2, E, T_2, T_{1\pm}\}$, scale towards zero in the thermodynamic limit in this phase (not shown). These two observations indicate that the low-temperature phase is non-magnetic with time reversal symmetry remaining intact down to the lowest temperatures. The symmetry-breaking transition is strongly first order, as revealed by the sharp jump in the energy density shown in Fig. 7(b). The sharp discontinuity at the transition makes it difficult to numerically extract the specific heat peak as defined in Eq. (9), i.e., from measuring energy fluctuations. As a more stable numerical approach, for the specific heat data shown in Fig. 7(b), we have used symmetric two-point numerical differentiation of the energy density. Furthermore, we note that, in the low-temperature limit, the specific heat plateaus towards 1 for all values of $J_{z\pm} \in (0.5, \sqrt{2})$ along the $A_2 \oplus T_1 \oplus T_2$ line, suggesting that thermal spin fluctuations about the ground-state configuration are purely quadratic. We emphasize that the position of the critical temperature T_c varies with $J_{z\pm}$, as shown in Fig. 4, eventually going to zero for $J_{z\pm} \rightarrow \sqrt{2}$, corresponding to the

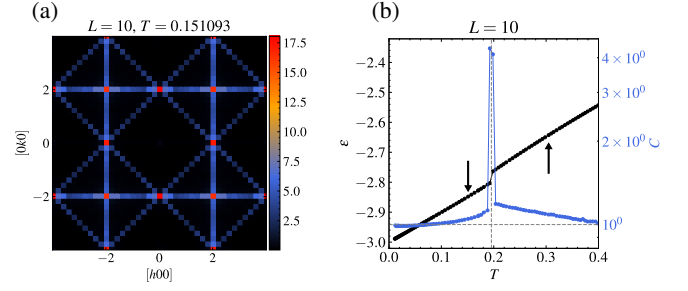


FIG. 7. (a) Static spin structure factor in the $[hk0]$ plane from classical Monte-Carlo simulations on an $L = 10$ lattice for a representative value of $J_{z\pm} = 1$ and fixed temperature $T = 0.15$ below T_c , describing the correlations in the spin nematic phase. (b) Energy density ε (black) and specific heat C (blue) as function of temperature for $J_{z\pm} = 1$, revealing the strong first-order nature of the spin-liquid-to-nematic transition, marked by the jump (sharp peak) in ε (C). Dashed line indicates the transition temperature. Arrows indicate the temperatures chosen in (a) and Fig. 5(d).

termination point of the $A_2 \oplus T_1 \oplus T_2$ line, identified with the antiferromagnetic Heisenberg model.²

Since the low-temperature phase for $J_{z\pm} > 0.5$ features no magnetic long-range order, the magnetic order parameters associated with the irreps, as defined in Eq. (10), are not suited to characterize this phase. However, the *distributions* of the magnitude of the irreps, calculated at the single-tetrahedron level, represent a useful quantity to understand the nature of the symmetry-broken ground state. Figures 8(a)-(c) show the A_2 , T_{1-} , and T_2 irrep magnitudes on each of the tetrahedra on an $L = 10$ lattice for a single Monte-Carlo snapshot, randomly selected from a simulation with $J_{z\pm} = 1$ at a temperature $T = 0.15$ below the transition temperature T_c . For this snapshot, the A_2 irrep has, on practically all tetrahedra, a significantly smaller magnitude in comparison with the T_{1-} and T_2 irreps. This suggests that out of the three competing orders A_2 , T_{1-} , and T_2 , the low-temperature phase is majorly built from only the T_{1-} and T_2 states. This observation can be further corroborated by considering histograms of the irreps across many Monte-Carlo snapshots, obtained from the simulation at a fixed temperature. The histograms of the A_2 , T_{1-} , and T_2 irrep magnitudes for $J_{z\pm} = 1$ and different temperatures above and below T_c , averaged over all tetrahedra for each snapshot, are shown in Figs. 8(d)-(f). Additionally, we report the temperature dependence of the average of these distributions in Fig. 8(g). The evolution of the histograms shows that lowering the temperature leads to a thermal depopulation of the A_2 irrep, reflected on the corresponding average magnitude of the A_2 irrep going to zero, see Figs. 8(d) and 8(g). In contrast, the T_{1-} and T_2 irreps acquire a finite average magnitude as suggested from the well-defined peaks in the histograms centered

² This termination point corresponds to a phase boundary between *four* antiferromagnetic orders, namely the A_2 , E , T_{1-} , and T_2 orders. The additional degeneracy with the E ordered phase at the termination point results in the transformation of the rank-2 Gauss's laws in Eq. (20) into the three rank-1 Gauss's laws of the antiferromagnetic Heisenberg model [9], ensuring the vanishing of the three components of the total magnetization vector.

at non-zero values. The behavior of the distributions suggests using the average of the single-tetrahedron irreps magnitude as an effective quantity to signal the onset of the low-temperature phase. Indeed, Fig. 8(g) reveals that these quantities indeed feature a clear jump around the transition temperature, with decreasing A_2 , and increasing T_2 and T_{1-} .³

The low-temperature state composed of T_2 and T_{1-} irreps is characterized by a specific behavior of the irreps components T_{1-}^α and T_2^α with $\alpha \in \{x, y, z\}$. Figures 9(a)-(c) show the distributions of the three different components of T_2 and T_{1-} irreps across the different tetrahedra of an $L = 10$ lattice, obtained from a single Monte-Carlo snapshot, randomly selected from a simulation at temperature $T = 0.15$ and $J_{z\pm} = 1$. The corresponding histograms across the different tetrahedra for the same Monte-Carlo snapshot are shown in Figs. 9(d)-(f). As is evident from these figures, one out of the three components $\{x, y, z\}$ of each of the two irreps is suppressed, where the suppressed component is the same for both irreps. For the Monte-Carlo snapshot shown, the component y has a smaller magnitude on each tetrahedron, and the corresponding histogram [Fig. 9(e)] is peaked around zero. The asymmetry between the distributions of the three irrep components indicates a spontaneous breaking of the cubic symmetry in the low-temperature phase. We have explicitly verified that other Monte-Carlo snapshots feature an analogous behavior, where the suppressed component varies between different snapshots, as required from the cubic symmetry of the model. The ground state manifold therefore falls into three disjoint sets characterized by suppressed x , y , or z components of the T_2 and T_{1-} irreps. However, each of these three sets contains a macroscopic number of degenerate states, reflected in the static spin structure factor, characterized by the absence of Bragg peaks and the presence of continuous intensity lines. For each set, these lines are oriented along a single direction, reflecting the spontaneous breaking of cubic spin symmetry.⁴ The extensive degeneracy in this phase can be exposed by studying the ground-state manifold whose states have all tetrahedra in a spin configuration defined by the T_{1-} and T_2 irreps. In the zero-temperature limit, for each tetrahedron, a continuous ground-state manifold can be constructed by linearly combining the *same* components of both the T_{1-} and T_2 irreps. The spin modes in this manifold are parametrized by $\mathbf{m}_\perp^\alpha(\theta) = \cos \theta \mathbf{m}_{T_{1-}}^\alpha + \sin \theta \mathbf{m}_{T_2}^\alpha$ for $\theta \in [0, 2\pi)$, which is analogous to the construction described in Ref. [22] involving a component of the E and T_{1-} irreps. To construct a lattice configuration from the \mathbf{m}_\perp^α single-tetrahedron states, one must tile these states while respecting the fact that adjacent tetrahedra share one spin. A straightforward lattice configuration resulting from this approach is a $\mathbf{q} = 0$ configuration, where all “up” tetrahedra adopt the same spin configuration $\mathbf{m}_\perp^\alpha(\theta)$. Alternatively, a *mixed* spin

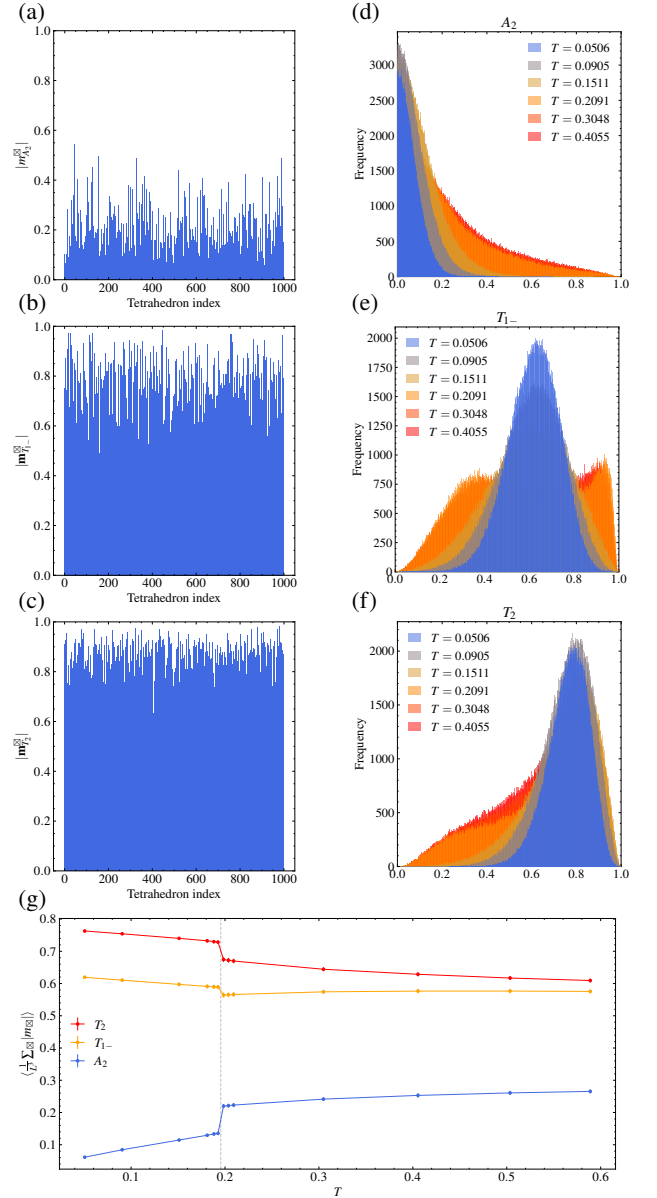


FIG. 8. (a) Distribution of the magnitude of the A_2 irrep across the different tetrahedra of an $L = 10$ lattice, obtained from a single Monte-Carlo snapshot, randomly selected from a simulation at temperature $T = 0.15$ and $J_{z\pm} = 1$. (b) Same as (a), but for the magnitude of the T_{1-} irrep. (c) Same as (a), but for the magnitude of the T_2 irrep. (d) Histogram of the magnitude of the A_2 irrep across many Monte-Carlo snapshots, obtained from Monte-Carlo simulations for $J_{z\pm} = 1$ and various fixed temperatures above and below T_c , averaged over all tetrahedra for each snapshot. (e) Same as (d), but for the magnitude of the T_{1-} irrep. (f) Same as (d), but for the magnitude of the T_2 irrep. (g) Monte-Carlo average of the single-tetrahedron A_2 , T_{1-} , and T_2 irreps magnitude as function of temperature. Dashed line indicates the transition temperature.

³ It is crucial to consider the magnitude $|\mathbf{m}_I^{\mathbf{q}}|$ of the irrep at the level of the single tetrahedron before averaging over the lattice, since $|\sum_{\mathbf{q}} \mathbf{m}_I^{\mathbf{q}}|$ vanishes in the thermodynamic limit due to the unbroken time reversal symmetry of the low-temperature state.

⁴ The three sets of lines in Fig. 7(a) arise in our Monte Carlo simulations due to the parallel tempering algorithm, which satisfies detailed balance and therefore uniformly samples across all symmetry-broken states.

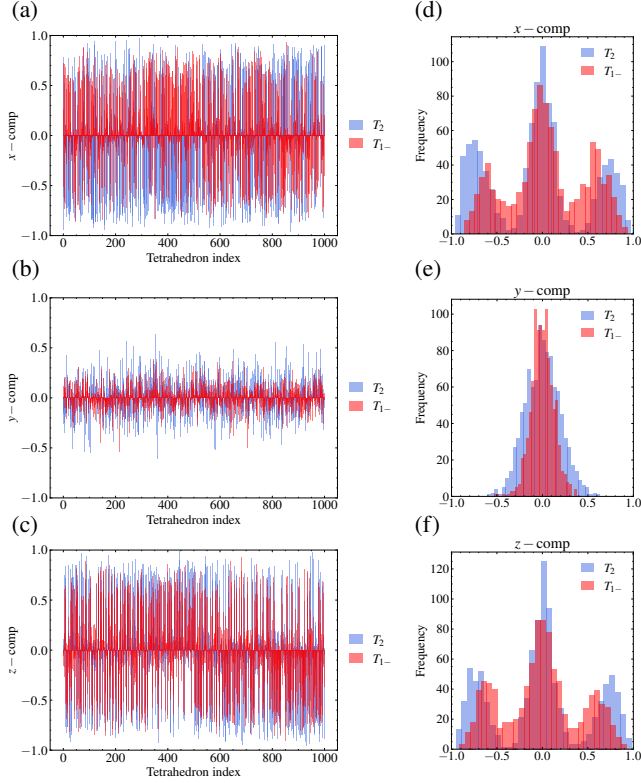


FIG. 9. (a) Distribution of the x component of the T_{1-} and T_2 irrep across the different tetrahedra of an $L = 10$ lattice, obtained from a single Monte-Carlo snapshot, randomly selected from a simulation at $T = 0.15$ and $J_{z\pm} = 1$. (b) Same as (a), but for the y components. (c) Same as (a), but for the z components. (d)-(f) Histograms of distributions shown in panels (a)-(c).

configuration can be created by tiling two distinct $m_{\perp}(\theta)$ spin

configurations, such as $m_{\perp}^{\alpha}(\theta_{\alpha})$ and $m_{\perp}^{\beta}(\theta_{\beta})$, where $\alpha \neq \beta$.⁵ This tiling requires specific values for the angles θ_{α} and θ_{β} , as evidenced by the intermediate values of the irrep components in the distributions shown in Figs. 9(d) and 9(f). We leave further details of the construction of full lattice configurations for future work.

The above analysis suggests that the low-temperature phase can be understood as a spin nematic with a local xy nature. In order to demonstrate that this is indeed the case, we show in Fig. 10 the single-site spin nematic order parameter Q_{\perp}^{site} , defined in Eq. (11), as function of temperature T , for a fixed representative value of $J_{z\pm} = 1$. The nematic order parameter vanishes in the paramagnetic phase and exhibits a distinct jump to a finite value at the first-order transition. Consequently, the

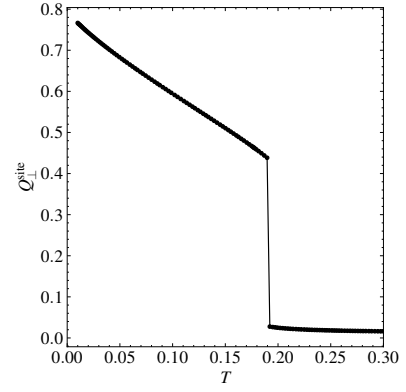


FIG. 10. Single-site nematic order parameter Q_{\perp}^{site} as function of temperature for $J_{z\pm}=1$ from classical Monte-Carlo simulations on an $L = 10$ lattice. The abrupt change at $T_c = 0.191(1)$ signals the onset of spin nematic order with a local xy nature.

low-temperature phase forms a spin nematic characterized by the breaking of cubic rotational symmetry. In this phase, spins fluctuate within the T_2 and T_{1-} irreps on local xy planes, while time-reversal symmetry remains intact down to the lowest temperatures.

C. Exposing the spin nematic using SCGA

The spin nematic phase observed in our classical Monte-Carlo simulations is not captured by a plain SCGA analysis at the $A_2 \oplus T_1 \oplus T_2$ line. In fact, in the plain SCGA analysis, the A_2 irrep is predicted to be thermally populated down to the lowest temperatures, in stark contrast to its sudden depopulation observed in the Monte-Carlo simulations. The depopulation of the A_2 irrep observed in the classical Monte-Carlo simulations suggests that the Ginzburg-Landau free energy functional at the $A_2 \oplus T_1 \oplus T_2$ line for $J_{z\pm} > 0.5$ contains higher-order terms, not captured by the SCGA analysis, that suppress the A_2 irrep for $J_{z\pm} > 0.5$. A naive way of including the depopulation of the A_2 irrep in the SCGA analysis would be to introduce a small energy cost to the A_2 irrep. However, simply adding an additional gap would neither reproduce the spin structure factors observed in the Monte-Carlo simulations nor expose the underlying physics of the selection. As an alternative approach, we investigate spin models defined in the vicinity of the $A_2 \oplus T_1 \oplus T_2$ line in a region where the A_2 irrep becomes gapped, while the T_{1-} and T_2 irreps remain degenerate. To this end, we relax the restrictions on the couplings J_{\pm} and $J_{\pm\pm}$ in Eq. (4) in order to parametrize a plane in coupling space at which the T_{1-} and T_2 states compete. Figure 11(a) shows the ground state phase diagram of the full model in Eq. (1) as function of J_{\pm} and $J_{\pm\pm}$ for fixed $J_{z\pm} = 1$ and $J_{zz} = -1$. The $A_2 \oplus T_1 \oplus T_2$ line discussed so far pierces the $J_{\pm}-J_{\pm\pm}$ phase diagram for fixed $J_{z\pm} = 1$ at the left-most corner of the A_2 phase, as indicated by the black dot in Fig. 11(a). The $A_2 \oplus T_1 \oplus T_2$ line

⁵ Constructing a mixed state with three spatial components is not feasible because the θ angles required to tile two distinct m_{\perp}^{α} states are not compatible, resulting in higher-energy configuration.

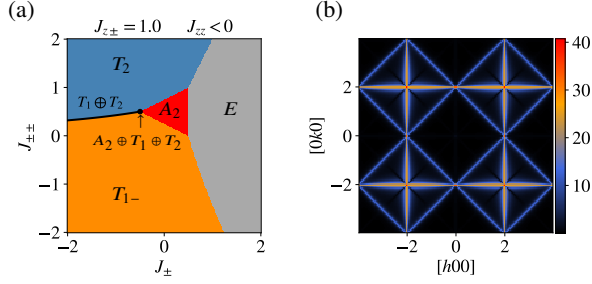


FIG. 11. (a) Ground state phase diagram of the full model in Eq. (1) as function of J_{\pm} and $J_{\pm\pm}$ for fixed $J_{z\pm} = 1$ and $J_{zz} = -1$. The $A_2 \oplus T_1 \oplus T_2$ line pierces the J_{\pm} - $J_{\pm\pm}$ phase diagram at the left-most corner of the A_2 phase, as indicated by the black dot. The intersection of the $T_1 \oplus T_2$ plane with the J_{\pm} - $J_{\pm\pm}$ phase diagram is marked as black line. (b) Static spin structure factor in the $[hk0]$ plane from SCGA in the low-temperature limit for the point $J_{z\pm} = 1$ and $J_{\pm} = -0.625$ on the $T_1 \oplus T_2$ plane, i.e., for $J_{\pm\pm}$ chosen according to Eq. (21), describing the correlations in the spin nematic phase.

connects to a $T_1 \oplus T_2$ plane⁶ located at the boundary between the T_{1-} and T_2 phases. The intersection between the $T_1 \oplus T_2$ plane and the J_{\pm} - $J_{\pm\pm}$ phase diagram is indicated by the black line in Fig. 11(a). The $T_1 \oplus T_2$ plane can be parametrized as function of J_{\pm} and $J_{z\pm}$ by

$$J_{\pm\pm} = \frac{1}{8} \left(2J_{\pm} + J_{zz} + \sqrt{4J_{\pm}^2 + 32J_{z\pm}^2 + 4J_{\pm}J_{zz} + 4J_{zz}^2} \right), \quad (21)$$

where

$$J_{\pm} < -\frac{J_{z\pm}^2}{J_{zz}} + \frac{3}{2}J_{zz}. \quad (22)$$

Figure 11(b) shows the static spin structure factor for a representative point on the $T_1 \oplus T_2$ plane. Remarkably, it exhibits continuous intensity lines just as those seen by the classical Monte-Carlo simulations in the spin nematic phase, cf. Fig. 7(a). We have explicitly verified that these features of the spin structure factor remain largely unchanged throughout the $T_1 \oplus T_2$ plane⁷. This suggests that the spin nematic phase observed at low temperatures in the classical Monte-Carlo simulations at the $A_2 \oplus T_1 \oplus T_2$ line for $J_{z\pm} > 0.5$ extends over the whole $T_1 \oplus T_2$ plane. In fact, we have explicitly confirmed this prediction of the SCGA analysis by classical Monte-Carlo simulations at a representative point $\{J_{zz}, J_{\pm}, J_{\pm\pm}, J_{z\pm}\} = \{-1, -0.7, \frac{\sqrt{59}-3}{10}, 1\}$ on the $T_1 \oplus T_2$ plane. The identification of the extended stability region of the spin nematic phase enables us to reinterpret the physics along the $A_2 \oplus T_1 \oplus T_2$ line as a competition between the A_2 antiferromagnet, stabilized within the central red triangle in Fig. 11(a),

and the spin nematic, stabilized along the $T_1 \oplus T_2$ plane. The outcome of this competition yields a classical spin liquid at intermediate temperatures, which ultimately is destabilized by a thermal ObD selection of a symmetry-breaking phase at low temperatures. The phase selected depends on the value of $J_{z\pm}$: our classical Monte Carlo simulations demonstrate that the A_2 phase is thermally selected for $J_{z\pm} < 0.5$, while the spin nematic phase is favored for $J_{z\pm} > 0.5$.

Having established the relation between the low-temperature phase observed along the $A_2 \oplus T_1 \oplus T_2$ line and the low-temperature phase in the $T_1 \oplus T_2$ plane, we use the SCGA analysis of the $T_1 \oplus T_2$ plane to rationalize the origin of the continuous intensity lines observed in the static spin structure factors in Figs. 7(b) and 11(b). Away from the $A_2 \oplus T_1 \oplus T_2$ line within the $T_1 \oplus T_2$ plane, the low-energy bands in the spectrum of the interaction matrix shown in Fig. 2 acquire a finite dispersion in the $[hk0]$ plane for all non-zero values of $J_{z\pm}$, but remain flat along the $[hhh]$, $[h00]$, and symmetry-related directions in reciprocal space.⁸ The existence of such flat lines in the spectrum of the interaction matrix implies that the degeneracy of the ground-state manifold for this phase scales at least linearly in size. We emphasize that the low-energy flat lines in the band spectrum are observed for *all* non-zero values of $J_{z\pm}$ and J_{\pm} in the $T_1 \oplus T_2$ plane. The low-energy flat lines in the spectra result in continuous lines of scattering in the SCGA spin structure factors, previously referred to as pinch lines [11], and observed in Fig. 11(b).

VII. CONCLUSIONS

In this work, we have studied the phase boundary between three $\mathbf{q} = 0$ states in the parameter space of a general bilinear nearest-neighbor Hamiltonian on the pyrochlore lattice. Such triple phase boundaries have recently attracted considerable attention as potential hosts for a variety of classical spin liquid phases [10, 14, 39]. Applying different analytical and numerical tools, we have constructed the finite-temperature phase diagram along the boundary between the A_2 (AIAO antiferromagnet), T_{1-} (splayed ferromagnet), and T_2 (Palmer-Chalker antiferromagnet) phases. For a fixed value of J_{zz} , this $A_2 \oplus T_1 \oplus T_2$ line can be parametrized by the interaction parameter $J_{z\pm}$. At high temperatures, and for all the models on the $A_2 \oplus T_1 \oplus T_2$ line, we observe a classical spin liquid regime at intermediate temperatures, where pinch-point features in the static spin structure factor develop. Through a self-consistent Gaussian approximation and an irreducible representation analysis, we show that these spin liquid regimes are described by a rank-1 U(1) theory for $J_{z\pm} = 0$, and a rank-2 U(1) theory for $J_{z\pm} \neq 0$. For all the models on the $A_2 \oplus T_1 \oplus T_2$ line, the spin liquid phase is destabilized at low temperatures by an order-by-disorder mechanism, resulting in the selection of a symmetry-broken phase. Using large-scale classical Monte-Carlo simulations, we have characterized the symmetry-broken

⁶ Due to the constraints in Eqs. (5) and (22), the $T_1 \oplus T_2$ “plane” is, geometrically, rather an infinitely-long finite-width strip with two parallel line boundaries in the width direction [Eq. (5)] and a single parabolic boundary in the length direction [Eq. (22)].

⁷ This excludes the case for which $J_{z\pm} = 0$ discussed in Ref. [10].

⁸ Interestingly, the bands of this model remain flat in the $[h\ell\ell]$ plane.

phases at low temperatures in detail and computed the finite-temperature phase diagram along the entire $A_2 \oplus T_1 \oplus T_2$ line. We have identified two distinct low-temperature phases, one for $J_{z\pm} < 0.5$ and another one for $J_{z\pm} > 0.5$. For $J_{z\pm} < 0.5$, we observe a continuous transition at a critical temperature T_c towards an AIAO $\mathbf{q} = 0$ antiferromagnet. The stabilization of a single $\mathbf{q} = 0$ phase below T_c down to the lowest temperatures is a scenario similar to those observed for $\text{Er}_2\text{Ti}_2\text{O}_7$ [3, 19] and $\text{Yb}_2\text{Ge}_2\text{O}_7$ [36]. For $J_{z\pm} \geq 0.5$ we identify a novel spin nematic phase at low temperatures, characterized by continuous lines of intensity in the spin structure factor. In contrast to the low- $J_{z\pm}$ case, the transition towards the spin nematic is strongly first order. The nematic phase features fluctuating components of the T_{1-} and T_2 irreps, with all other modes being thermally depopulated. It exhibits three macroscopically-degenerate sets of ground states mutually associated by cubic symmetry. The three distinct sets are characterized by the suppression of a different component of the T_{1-} and T_2 irreps in each case.

The identification of the order-by-disorder-selected nematic phase along the $A_2 \oplus T_1 \oplus T_2$ line led us to uncover a two-dimensional $T_{1-} \oplus T_2$ plane in coupling space, spanned by the parameters $J_{z\pm}$ and J_{\pm} , along which the nematic state is stabilized. To the best of our knowledge, the nematic phase discovered along this line represents the first instance of a non-magnetic, yet symmetry-broken state arising from a low-temperature instability of a higher-rank classical spin liquid state. In the limit $J_{z\pm} \rightarrow 0$, it connects to the nematic state observed as the low-temperature instability of the rank-1 classical spin liquid in Ref. [10]. Our work thus significantly expands the range of magnetic phases resultant of an entropic selection, which otherwise previously only included $\mathbf{q} = 0$ phases [3, 21, 22], and in the most exotic cases certain classical spin liquids [14].

In the future, it would be interesting to study the effects of quantum fluctuations on the nematic state found in the classical limit. This question could be approached by pseudo-fermion or pseudo-majorana functional renormalization group approaches [51–54], or potentially within a high-temperature series expansion [55, 56]. Quantum effects could introduce an even more increased level of complexity in the competition between the various states involved, potentially leading to further exotic phases of matter.

Our results for the $A_2 \oplus T_1 \oplus T_2$ line suggest that similarly rich physics may be at work also at other triple phase boundaries, such as the $A_2 \oplus T_2 \oplus T_E$ line, corresponding to the upper corner of the red triangle in Fig. 11(a), or the $A_2 \oplus T_1 \oplus T_E$ line, corresponding to the lower right corner of the red triangle in Fig. 11(a). These questions will be addressed in a separate paper.

Appendix A: Irreducible representations

In this appendix, we provide the explicit form of the irreducible representation spin modes and their single-tetrahedron energies as a function of the interaction couplings $\{J_{zz}, J_{\pm}, J_{\pm\pm}, J_{z\pm}\}$. The five single-tetrahedron irreps \mathbf{m}_I are

given in terms of spins by

$$\mathbf{m}_{A_2} = \frac{1}{4} \sum_{\mu} \mathbf{S}_{\mu} \cdot \hat{\mathbf{z}}_{\mu}, \quad (\text{A1})$$

$$\mathbf{m}_E = \frac{1}{4} \sum_{\mu} \begin{pmatrix} \mathbf{S}_{\mu} \cdot \hat{\mathbf{x}}_{\mu} \\ \mathbf{S}_{\mu} \cdot \hat{\mathbf{y}}_{\mu} \end{pmatrix}, \quad (\text{A2})$$

$$\mathbf{m}_{T_2} = \frac{1}{4} \sqrt{\frac{3}{2}} \sum_{\mu} \hat{\mathbf{z}}_{\mu} \times \mathbf{S}_{\mu}, \quad (\text{A3})$$

$$\mathbf{m}_{T_{1,\parallel}} = \frac{1}{4} \sum_{\mu} \mathbf{S}_{\mu}, \quad (\text{A4})$$

$$\mathbf{m}_{T_{1,\perp}} = \frac{\sqrt{3}}{4} \sum_{\mu} \begin{pmatrix} \hat{z}_{\mu}^x \mathbf{v}_{\mu}^{yz} \cdot \mathbf{S}_{\mu} \\ \hat{z}_{\mu}^y \mathbf{v}_{\mu}^{xz} \cdot \mathbf{S}_{\mu} \\ \hat{z}_{\mu}^z \mathbf{v}_{\mu}^{xy} \cdot \mathbf{S}_{\mu} \end{pmatrix}, \quad (\text{A5})$$

where $\mu = 0, \dots, 3$ specifies the sublattice index for each point in the tetrahedron [34]. The normalization is chosen to give a unit magnitude if the corresponding irrep is realized. The vectors $\hat{\mathbf{x}}_{\mu}, \hat{\mathbf{y}}_{\mu}, \hat{\mathbf{z}}_{\mu}$ refer to the local orthonormal cubic coordinate frame associated to the site of sublattice μ . For example, for $\mu = 0$ we have

$$\hat{\mathbf{x}}_0 = \frac{1}{\sqrt{6}} \begin{pmatrix} -1 \\ -1 \\ 2 \end{pmatrix}, \quad \hat{\mathbf{y}}_0 = \frac{1}{\sqrt{2}} \begin{pmatrix} 1 \\ -1 \\ 0 \end{pmatrix}, \quad \hat{\mathbf{z}}_0 = \frac{1}{\sqrt{3}} \begin{pmatrix} 1 \\ 1 \\ 1 \end{pmatrix}, \quad (\text{A6})$$

where the components are expressed in a global cartesian coordinate frame. The vectors $\mathbf{v}^{\alpha\beta}$ are the normalized bond vectors attached to a sublattice μ and lying on the α - β plane,

$$\begin{aligned} \mathbf{v}_0^{xy} &= \frac{1}{\sqrt{2}} \begin{pmatrix} 1 \\ 1 \\ 0 \end{pmatrix}, & \mathbf{v}_1^{xy} &= -\mathbf{v}_0^{xy}, \\ \mathbf{v}_2^{xy} &= \frac{1}{\sqrt{2}} \begin{pmatrix} 1 \\ -1 \\ 0 \end{pmatrix}, & \mathbf{v}_3^{xy} &= -\mathbf{v}_2^{xy}, \\ \mathbf{v}_0^{xz} &= \frac{1}{\sqrt{2}} \begin{pmatrix} 1 \\ 0 \\ 1 \end{pmatrix}, & \mathbf{v}_2^{xz} &= -\mathbf{v}_0^{xz}, \\ \mathbf{v}_1^{xz} &= \frac{1}{\sqrt{2}} \begin{pmatrix} 1 \\ 0 \\ -1 \end{pmatrix}, & \mathbf{v}_3^{xz} &= -\mathbf{v}_1^{xz}, \\ \mathbf{v}_0^{yz} &= \frac{1}{\sqrt{2}} \begin{pmatrix} 0 \\ 1 \\ 1 \end{pmatrix}, & \mathbf{v}_3^{yz} &= -\mathbf{v}_0^{yz}, \\ \mathbf{v}_1^{yz} &= \frac{1}{\sqrt{2}} \begin{pmatrix} 0 \\ 1 \\ -1 \end{pmatrix}, & \mathbf{v}_2^{yz} &= -\mathbf{v}_1^{yz}. \end{aligned} \quad (\text{A7})$$

The generic single-tetrahedron Hamiltonian can be written as [34]

$$\begin{aligned} \mathcal{H}_{\boxtimes} &= a_{A_2} \mathbf{m}_{A_2}^2 + a_E \mathbf{m}_E^2 + a_{T_2} \mathbf{m}_{T_2}^2 \\ &+ a_{T_{1,\parallel}} \mathbf{m}_{T_{1,\parallel}}^2 + a_{T_{1,\perp}} \mathbf{m}_{T_{1,\perp}}^2 + a_{T_{1,\text{mix}}} \mathbf{m}_{T_{1,\parallel}} \cdot \mathbf{m}_{T_{1,\perp}}, \end{aligned} \quad (\text{A8})$$

where each irreducible representation is associated with an energy a_I . Note that the coefficient $a_{T_1, \text{mix}}$ quantifies the mixing between the two T_1 irreps. Each coefficient in Eq. (A8) is expressed as a function of the couplings as [47]

$$\begin{aligned} a_{A_2} &= 3J_{zz}, \quad a_E = -6J_{\pm}, \quad a_{T_2} = 2J_{\pm} - 4J_{\pm\pm}, \\ a_{T_1, \parallel} &= \frac{1}{3} \left(-J_{zz} + 4J_{\pm} + 8J_{\pm\pm} + 8\sqrt{2}J_{z\pm} \right), \\ a_{T_1, \perp} &= \frac{1}{3} \left(-2J_{zz} + 2J_{\pm} + 4J_{\pm\pm} - 8\sqrt{2}J_{z\pm} \right), \\ a_{T_1, \text{mix}} &= -\frac{\sqrt{2}}{3} \left(-J_{zz} - 2J_{\pm} - 4J_{\pm\pm} + 2\sqrt{2}J_{z\pm} \right). \end{aligned} \quad (\text{A9})$$

In order to avoid the mixing between the two T_1 irreps, one can define a new rotated irrep basis, namely

$$\begin{pmatrix} \mathbf{m}_{T_1-} \\ \mathbf{m}_{T_1+} \end{pmatrix} = \begin{pmatrix} \cos \phi & -\sin \phi \\ \sin \phi & \cos \phi \end{pmatrix} \begin{pmatrix} \mathbf{m}_{T_1, \parallel} \\ \mathbf{m}_{T_1, \perp} \end{pmatrix}, \quad (\text{A10})$$

where the rotation angle is defined by

$$\tan 2\phi = \frac{a_{T_1, \text{mix}}}{a_{T_1, \perp} - a_{T_1, \parallel}}. \quad (\text{A11})$$

Following the transformation, the Hamiltonian takes the form shown in Eq. (3), with no mixing terms in the T_1 irreps and single-tetrahedron energies given by

$$a_{T_{1\pm}} = \frac{1}{2} \left(a_{T_1, \perp} + a_{T_1, \parallel} \pm \sqrt{(a_{T_1, \perp} - a_{T_1, \parallel})^2 + a_{T_1, \text{mix}}^2} \right). \quad (\text{A12})$$

Appendix B: Classical low-temperature expansion

In this appendix, we provide a brief overview of the classical low-temperature expansion and its application to the $A_2 \oplus T_1 \oplus T_2$ line for the case $J_{z\pm} = 0$. The classical low-temperature expansion is an analytical method that examines fluctuations around a ground state configuration by studying an effective low-temperature Hamiltonian. This effective Hamiltonian is obtained by expressing the classical spin vectors as small fluctuations about the ground state, namely

$$\mathbf{S}_i \simeq \left(\delta n_i^{\tilde{x}}, \delta n_i^{\tilde{y}}, S \left(1 - \frac{(\delta n_i^{\tilde{x}})^2}{2S^2} - \frac{(\delta n_i^{\tilde{y}})^2}{2S^2} \right) \right), \quad (\text{B1})$$

where the basis $\{\tilde{x}, \tilde{y}, \tilde{z}\}$ is chosen such that the \tilde{z}_i axis aligns with the selected ground state spin configuration at a given pyrochlore lattice site i . Substituting Eq. (B1) into the Hamiltonian given by Eq. (1) under the assumption that $\delta n^\alpha \ll 1$, we obtain an 8×8 Hamiltonian acting on the spin fluctuations δn^α , denoted $\mathcal{H}^{(2)}$, which can be diagonalized. For more details on this method, we refer to Ref. [22].

As discussed in the main text, the application of a classical low-temperature expansion to the $A_2 \oplus T_1 \oplus T_2$ line for the case $J_{z\pm} = 0$ leads to the observation of four zero-energy flat bands in the spectrum of $\mathcal{H}^{(2)}$, see Fig. 12. At the present order of the expansion, the zero-energy bands can be understood to describe higher-order modes. If these modes are considered to be

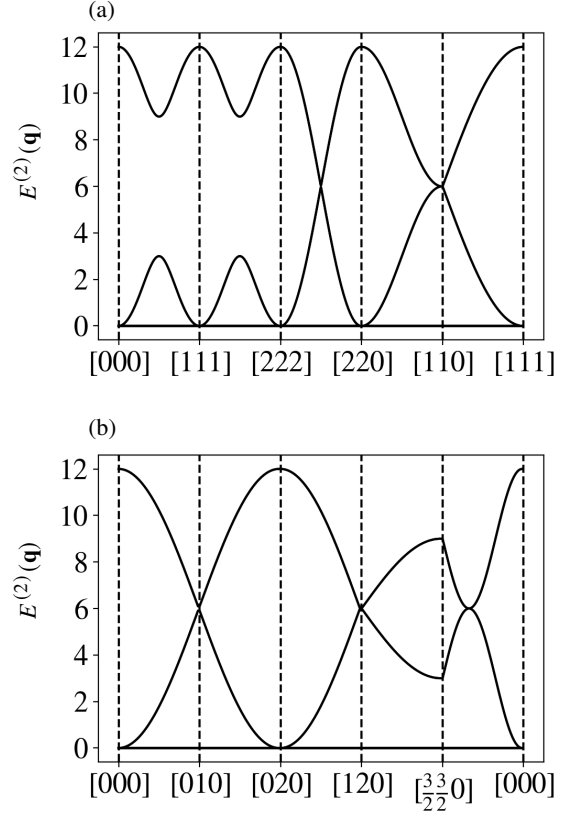


FIG. 12. Spectrum of the effective Hamiltonian $\mathcal{H}^{(2)}$ in the classical low-temperature expansion about the A_2 phase in the non-Kramers case for $J_{z\pm} = 0$ along high-symmetry paths in (a) the $[hhl]$ plane and (b) the $[hk0]$ plane in reciprocal space. The dispersive bands are twofold degenerate, while the zero-energy bands are fourfold degenerate.

quartic, the equipartition theorem predicts a low-temperature specific heat of $3/4$, consistent with the classical Monte-Carlo results.

Appendix C: Specific heat in the AIAO phase of the Kramers Hamiltonian

In this appendix, we show, using classical Monte-Carlo simulations, that the specific heat approaches one in the low-temperature limit of the A_2 phase in the Kramers case for $J_{z\pm} \in (0, 0.5)$. Upon cooling below T_c , the specific heat initially drops below one, as illustrated in Fig. 6(a). However, in the Kramers case for $J_{z\pm} \neq 0$, the classical low-temperature expansion now features eight dispersive bands at the quadratic order for the AIAO phase, in contrast to the non-Kramers case for $J_{z\pm} = 0$, thus predicting a specific heat value of one at low temperatures. Indeed, pushing the classical Monte-Carlo simulations down to temperatures as small as $T = 10^{-4}$, the upturn of the specific heat toward $C = 1$ becomes visible, see Fig. 13. All curves for $J_{z\pm} \geq 0.2$ converge at the predicted value $C(T \rightarrow 0) = 1$ at the lowest temperatures. The fact

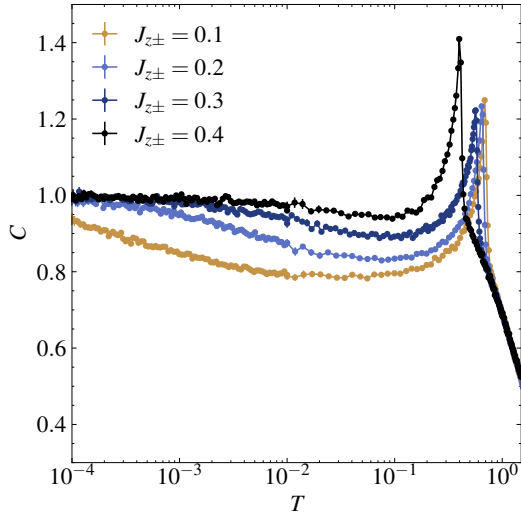


FIG. 13. Specific heat as function of temperature in a linear-log plot from classical Monte-Carlo simulations on an $L = 10$ lattice for different values of $J_{z\pm}$, indicating that $C(T \rightarrow 0) = 1$ in the A_2 phase of the Kramers Hamiltonian for $J_{z\pm} \neq 0$.

that the curve for $J_{z\pm} = 0.1$ requires even smaller temperatures in order to observe convergence can be explained by the smaller bandwidth of the lowest-energy modes in the classical low-temperature expansion. The same argument explains the behavior of the curves for different $J_{z\pm}$. Indeed, the band dispersion of the lowest mode monotonically increases with increasing $J_{z\pm}$ (not shown). Hence, the temperature regime for which the specific heat is one also increases with $J_{z\pm}$, as evident in Fig. 13.

Appendix D: Neutron structure factors

In this appendix, we provide SCGA neutron structure factors for both polarized and unpolarized cases in the classical spin liquid and spin nematic phases, to facilitate comparison with future experiments. We define the unpolarized neutron structure factor as

$$S_{\perp}(\mathbf{q}) = \sum_{\alpha\beta} \sum_{\mu\nu} \left(\delta_{\alpha\beta} - \frac{q^{\alpha} q^{\beta}}{q^2} \right) \langle S_{\mu}^{\alpha}(-\mathbf{q}) S_{\nu}^{\beta}(\mathbf{q}) \rangle, \quad (\text{D1})$$

and the non-spin-flip and spin-flip neutron structure factors as

$$S_{\perp}^{\text{NSF}}(\mathbf{q}) = \sum_{\alpha\beta} \sum_{\mu\nu} z_s^{\alpha} z_s^{\beta} \langle S_{\mu}^{\alpha}(-\mathbf{q}) S_{\nu}^{\beta}(\mathbf{q}) \rangle, \quad (\text{D2})$$

and

$$S_{\perp}^{\text{SF}}(\mathbf{q}) = S_{\perp}(\mathbf{q}) - S_{\perp}^{\text{NSF}}(\mathbf{q}), \quad (\text{D3})$$

respectively. In the above equations, the indices α and β label the spin components, while μ and ν are sublattice indices, and z_s corresponds to the polarization direction of the incident neutron. We consider structure factors in the $[hk0]$ plane in

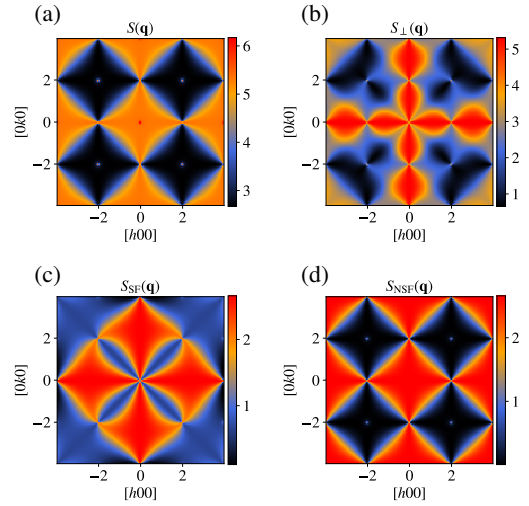


FIG. 14. (a) Static spin structure factor in the $[hk0]$ plane from SCGA in the low-temperature limit in the non-Kramers case $J_{z\pm} = 0$ on the $A_2 \oplus T_1 \oplus T_2$ line, describing the correlations in the rank-1 classical spin liquid. [Same as Fig. 3(a) in the main text.] (b) Same as (a), but showing the unpolarized neutron structure factor. (c) Same as (a), but showing the polarized neutron structure factor in the spin-flip channel. (d) Same as (a), but showing the polarized neutron structure factor in the non-spin-flip channel.

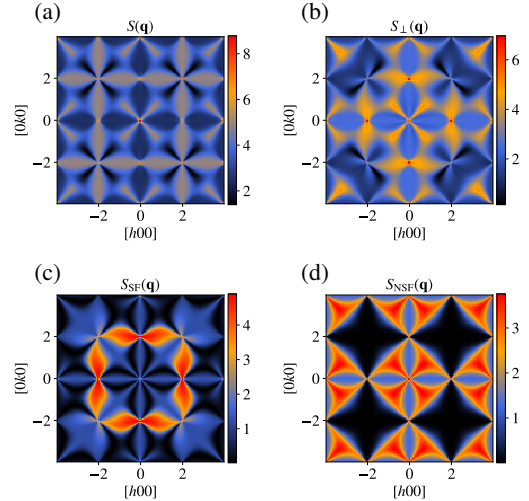


FIG. 15. Same as Fig. 14, but in the Kramers case for a representative small value of $J_{z\pm} = 0.4$, describing the correlations in the rank-2 classical spin liquid.

reciprocal space, as these are the ones where fourfold pinch points can be observed. Figure 14 shows the spin structure factor together with the neutron structure factors for the rank-1 classical spin liquid in the non-Kramers case for $J_{z\pm} = 0$. For comparison, the spin and neutron structure factors in the rank-2 classical spin liquid in the Kramers case for two representative values of $J_{z\pm} = 0.4$ and $J_{z\pm} = 1.0$ on the $A_2 \oplus T_1 \oplus T_2$ line are shown in Figs. 15 and 16. Finally, Fig. 17 shows the spin and neutron structure factors for the spin nematic phase in the

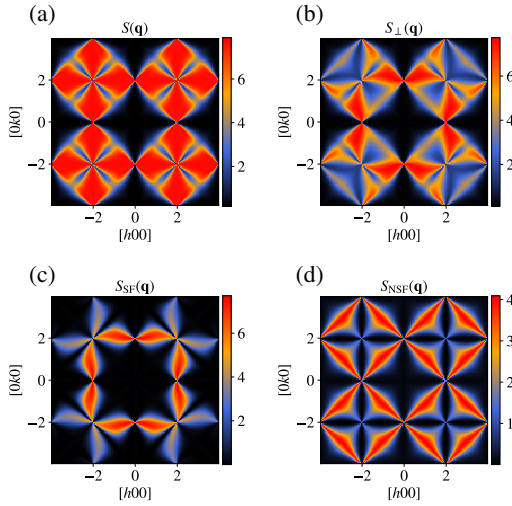


FIG. 16. Same as Fig. 14, but in the Kramers case for a representative large value of $J_{z\pm} = 1$, describing the correlations in the rank-2 classical spin liquid.

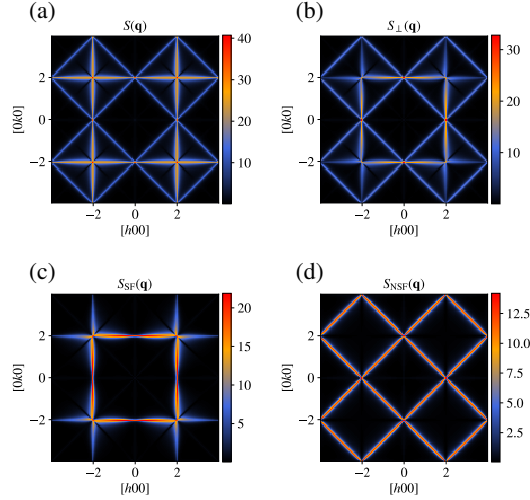


FIG. 17. Same as Fig. 14, but in the Kramers case for a representative value of $J_{z\pm} = 1$ and $J_{\pm} = -0.625$ on the $T_1 \oplus T_2$ plane, describing the correlations in the spin nematic phase.

non-Kramers case for a representative value of $J_{z\pm} = 1$ and $J_{\pm} = -0.625$ on the $T_1 \oplus T_2$ plane.

ACKNOWLEDGMENTS

We thank Michel J. P. Gingras, Han Yan, Owen Benton, Ludovic Jaubert, Johannes Reuther, Yasir Iqbal, Kristian Chung, and Matthias Vojta for insightful discussions. This work has been supported by the Deutsche Forschungsgemeinschaft (DFG) through SFB 1143 (A07, Project No. 247310070), the Würzburg-Dresden Cluster of Excellence *ct.qmat* (EXC 2147, Project No. 390858490), and the Emmy Noether program (JA2306/4-1, Project No. 411750675). DLG acknowledges financial support from the DFG through the Hallwachs-Röntgen Postdoc Program of *ct.qmat* (EXC 2147, Project No. 390858490). The authors gratefully acknowledge the computing time made available to them on the high-performance computer at the NHR Center of TU Dresden. This center is jointly supported by the German Federal Ministry of Education and Research and the state governments participating in the NHR [42].

-
- [1] C. Lacroix, P. Mendels, and F. Mila, *Introduction to Frustrated Magnetism* (Springer, 2011).
 - [2] L. Balents, Spin liquids in frustrated magnets, *Nature* **464**, 199 (2010).
 - [3] L. Savary, K. A. Ross, B. D. Gaulin, J. P. C. Ruff, and L. Balents, Order by Quantum Disorder in $\text{Er}_2\text{Ti}_2\text{O}_7$, *Phys. Rev. Lett.* **109**, 167201 (2012).
 - [4] P. Nikolić and T. Senthil, Theory of the kagome lattice Ising antiferromagnet in weak transverse fields, *Phys. Rev. B* **71**, 024401 (2005).
 - [5] J. G. Rau and M. J. P. Gingras, Frustrated Quantum Rare-Earth Pyrochlores, *Annu. Rev. Condens. Matter Phys.* (2018).
 - [6] S. Trebst and C. Hickey, Kitaev materials, *Phys. Rep.* **950**, 1 (2022).
 - [7] C. Castelnovo, R. Moessner, and S. L. Sondhi, Magnetic monopoles in spin ice, *Nature* **451**, 42 (2008).
 - [8] H. Yan, O. Benton, L. D. C. Jaubert, and N. Shannon, Rank-2 $U(1)$ Spin Liquid on the Breathing Pyrochlore Lattice, *Phys. Rev. Lett.* **124**, 127203 (2020).
 - [9] R. Moessner and J. T. Chalker, Properties of a Classical Spin Liquid: The Heisenberg Pyrochlore Antiferromagnet, *Phys. Rev. Lett.* **80**, 2929 (1998).
 - [10] M. Taillefumier, O. Benton, H. Yan, L. D. C. Jaubert, and N. Shannon, Competing Spin Liquids and Hidden Spin-Nematic

- Order in Spin Ice with Frustrated Transverse Exchange, *Phys. Rev. X* **7**, 041057 (2017).
- [11] O. Benton, L. D. C. Jaubert, H. Yan, and N. Shannon, A spin-liquid with pinch-line singularities on the pyrochlore lattice, *Nat. Commun.* **7**, 11572 (2016).
- [12] O. Benton, O. Sikora, and N. Shannon, Seeing the light: Experimental signatures of emergent electromagnetism in a quantum spin ice, *Phys. Rev. B* **86**, 075154 (2012).
- [13] E. M. Smith, O. Benton, D. R. Yahne, B. Placke, R. Schäfer, J. Gaudet, J. Dudemaine, A. Fitterman, J. Beare, A. R. Wildes, S. Bhattacharya, T. DeLazzer, C. R. C. Buhariwalla, N. P. Butch, R. Movshovich, J. D. Garrett, C. A. Marjerrison, J. P. Clancy, E. Kermarrec, G. M. Luke, A. D. Bianchi, K. A. Ross, and B. D. Gaulin, Case for a $U(1)_\pi$ Quantum Spin Liquid Ground State in the Dipole-Octupole Pyrochlore $\text{Ce}_2\text{Zr}_2\text{O}_7$, *Phys. Rev. X* **12**, 021015 (2022).
- [14] D. Lozano-Gómez, V. Noculak, J. Oitmaa, R. R. P. Singh, Y. Iqbal, J. Reuther, and M. J. P. Gingras, Competing gauge fields and entropically driven spin liquid to spin liquid transition in non-Kramers pyrochlores, *Proc. Nat. Acad. Sci.* **121**, e2403487121 (2024).
- [15] K. T. K. Chung and M. J. P. Gingras, 2-Form $U(1)$ Spin Liquids: Classical Model and Quantum Aspects, *arXiv:2310.17607*.
- [16] D. Lozano-Gomez, Y. Iqbal, and M. Vojta, A Classical Chiral Spin-Liquid from Chiral Interactions on the Pyrochlore Lattice, *arXiv:2403.10601*.
- [17] J. Villain, R. Bidaux, J.-P. Carton, and R. Conte, Order as an effect of disorder, *J. Phys. France*, **41**, 1263 (1980).
- [18] E. Belorizky, R. Casalegno, and J. J. Niez, Calculation of the Spin Wave Energy Gap at $k = 0$ for a Simple Cubic Ferromagnet with Anisotropic Exchange Interactions, *Phys. Status Solidi B* **102**, 365 (1980).
- [19] M. E. Zhitomirsky, M. V. Gvozdkova, P. C. W. Holdsworth, and R. Moessner, Quantum Order by Disorder and Accidental Soft Mode in $\text{Er}_2\text{Ti}_2\text{O}_7$, *Phys. Rev. Lett.* **109**, 077204 (2012).
- [20] M. E. Zhitomirsky and A. L. Chernyshev, *Colloquium* : Spontaneous Magnon Decays, *Rev. Mod. Phys.* **85**, 219 (2013).
- [21] G.-W. Chern, Pyrochlore antiferromagnet with antisymmetric exchange interactions: critical behavior and order from disorder, *arXiv:1008.3038*.
- [22] V. Noculak, D. Lozano-Gómez, J. Oitmaa, R. R. P. Singh, Y. Iqbal, M. J. P. Gingras, and J. Reuther, Classical and quantum phases of the pyrochlore $S = \frac{1}{2}$ magnet with Heisenberg and Dzyaloshinskii-Moriya interactions, *Phys. Rev. B* **107**, 214414 (2023).
- [23] A. Hickey, D. Lozano-Gómez, and M. J. P. Gingras, A Classical Chiral Spin-Liquid from Chiral Interactions on the Pyrochlore Lattice, *arXiv:2403.02391*.
- [24] M. E. Brooks-Bartlett, S. T. Banks, L. D. Jaubert, A. Harman-Clarke, and P. C. Holdsworth, Magnetic-moment fragmentation and monopole crystallization, *Phys. Rev. X* **4**, 011007 (2014).
- [25] S. Petit, E. Lhotel, B. Canals, M. Ciomaga Hatnean, J. Ollivier, H. Mutka, E. Ressouche, A. R. Wildes, M. R. Lees, and G. Balakrishnan, Observation of magnetic fragmentation in spin ice, *Nat. Phys.* **12**, 746 (2016).
- [26] O. Benton, Quantum origins of moment fragmentation in $\text{Nd}_2\text{Zr}_2\text{O}_7$, *Phys. Rev. B* **94**, 104430 (2016).
- [27] Y. Onose, T. Ideue, H. Katsura, Y. Shiomi, N. Nagaosa, and Y. Tokura, Observation of the Magnon Hall Effect, *Science* **329**, 297 (2010).
- [28] H. Yan, O. Benton, R. Moessner, and A. H. Nevidomskyy, Classification of classical spin liquids: Typology and resulting landscape, *Phys. Rev. B* **110**, L020402 (2024).
- [29] K. T. K. Chung, J. S. K. Goh, A. Mukherjee, W. Jin, D. Lozano-Gómez, and M. J. P. Gingras, Probing Flat Band Physics in Spin Ice Systems via Polarized Neutron Scattering, *Phys. Rev. Lett.* **128**, 107201 (2022).
- [30] K. A. Ross, L. Savary, B. D. Gaulin, and L. Balents, Quantum Excitations in Quantum Spin Ice, *Phys. Rev. X* **1**, 021002 (2011).
- [31] A. Sadeghi, M. Alaei, F. Shahbazi, and M. J. P. Gingras, Spin Hamiltonian, Order out of a Coulomb Phase, and Pseudocriticality in the Frustrated Pyrochlore Heisenberg Antiferromagnet FeF_3 , *Phys. Rev. B* **91**, 140407 (2015).
- [32] S. E. Palmer and J. T. Chalker, Order induced by dipolar interactions in a geometrically frustrated antiferromagnet, *Phys. Rev. B* **62**, 488 (2000).
- [33] J. D. Thompson, P. A. McClarty, D. Prabhakaran, I. Cabrera, T. Guidi, and R. Coldea, Quasiparticle Breakdown and Spin Hamiltonian of the Frustrated Quantum Pyrochlore $\text{Yb}_2\text{Ti}_2\text{O}_7$ in a Magnetic Field, *Phys. Rev. Lett.* **119**, 057203 (2017).
- [34] H. Yan, O. Benton, L. Jaubert, and N. Shannon, Theory of multiple-phase competition in pyrochlore magnets with anisotropic exchange with application to $\text{Yb}_2\text{Ti}_2\text{O}_7$, $\text{Er}_2\text{Ti}_2\text{O}_7$, and $\text{Er}_2\text{Sn}_2\text{O}_7$, *Phys. Rev. B* **95**, 094422 (2017).
- [35] P. A. McClarty, S. H. Curnoe, and M. J. P. Gingras, Energetic selection of ordered states in a model of the $\text{Er}_2\text{Ti}_2\text{O}_7$ frustrated pyrochlore XY antiferromagnet, *J. Phys. Conf. Ser.* **145**, 012032 (2009).
- [36] C. L. Sarkis, J. G. Rau, L. D. Sanjeewa, M. Powell, J. Kolis, J. Marbey, S. Hill, J. A. Rodriguez-Rivera, H. S. Nair, D. R. Yahne, S. Säubert, M. J. P. Gingras, and K. A. Ross, Unraveling competing microscopic interactions at a phase boundary: A single-crystal study of the metastable antiferromagnetic pyrochlore $\text{Yb}_2\text{Ge}_2\text{O}_7$, *Phys. Rev. B* **102**, 134418 (2020).
- [37] D. R. Yahne, D. Pereira, L. D. C. Jaubert, L. D. Sanjeewa, M. Powell, J. W. Kolis, G. Xu, M. Enjalran, M. J. P. Gingras, and K. A. Ross, Understanding Reentrance in Frustrated Magnets: The Case of the $\text{Er}_2\text{Sn}_2\text{O}_7$ Pyrochlore, *Phys. Rev. Lett.* **127**, 277206 (2021).
- [38] A. W. Wong, Z. Hao, and M. J. Gingras, Ground state phase diagram of generic XY pyrochlore magnets with quantum fluctuations, *Phys. Rev. B* **88**, 144402 (2013).
- [39] D. Lozano-Gómez, O. Benton, M. J. P. Gingras, and H. Yan, Atlas of Classical Pyrochlore Spin Liquids, in preparation.
- [40] S. V. Isakov, K. Gregor, R. Moessner, and S. L. Sondhi, Dipolar Spin Correlations in Classical Pyrochlore Magnets, *Phys. Rev. Lett.* **93**, 167204 (2004).
- [41] P. H. Conlon and J. T. Chalker, Absent pinch points and emergent clusters: Further neighbor interactions in the pyrochlore Heisenberg antiferromagnet, *Phys. Rev. B* **81**, 224413 (2010).
- [42] Computations were performed on the BARNARD clusters of NHR@TUD, <https://www.nhr-verein.de>.
- [43] N. Shannon, T. Momoi, and P. Sindzingre, Nematic Order in Square Lattice Frustrated Ferromagnets, *Phys. Rev. Lett.* **96**, 027213 (2006).
- [44] A. Smerald, H. T. Ueda, and N. Shannon, Theory of inelastic neutron scattering in a field-induced spin-nematic state, *Phys. Rev. B* **91**, 174402 (2015).
- [45] N. Francini and L. Janssen, Spin vestigial orders in extended Heisenberg-Kitaev models near hidden $SU(2)$ points: Application to $\text{Na}_2\text{Co}_2\text{TeO}_6$, *Phys. Rev. B* **109**, 075104 (2024).
- [46] S. Petit, E. Lhotel, S. Guitteny, O. Florea, J. Robert, P. Bonville, I. Mirebeau, J. Ollivier, H. Mutka, E. Ressouche, C. Decorse, M. Ciomaga Hatnean, and G. Balakrishnan, Antiferroquadrupolar correlations in the quantum spin ice candidate $\text{Pr}_2\text{Zr}_2\text{O}_7$, *Phys. Rev. B* **94**, 165153 (2016).

- [47] O. Benton, Classical and quantum spin liquids on the pyrochlore lattice, Ph.D. thesis, University of Bristol, (2014).
- [48] N. Davier, F. A. Gómez Albarracín, H. D. Rosales, and P. Pujol, Combined approach to analyze and classify families of classical spin liquids, *Phys. Rev. B* **108**, 054408 (2023).
- [49] M. Pretko, Subdimensional particle structure of higher rank $U(1)$ spin liquids, *Phys. Rev. B* **95**, 115139 (2017).
- [50] M. Pretko, The fracton gauge principle, *Phys. Rev. B* **98**, 115134 (2018).
- [51] B. Schneider, J. Reuther, M. G. Gonzalez, B. Sbierski, and N. Niggemann, Temperature flow in pseudo-Majorana functional renormalization for quantum spins, *Phys. Rev. B* **109**, 195109 (2024).
- [52] N. Niggemann, Y. Iqbal, and J. Reuther, Quantum Effects on Unconventional Pinch Point Singularities, *Phys. Rev. Lett.* **130**, 196601 (2023).
- [53] T. Müller, D. Kiese, N. Niggemann, B. Sbierski, J. Reuther, S. Trebst, R. Thomale, and Y. Iqbal, Pseudo-fermion functional renormalization group for spin models, *Rep. Progr. Phys.* **87**, 036501 (2024).
- [54] V. Noculak and J. Reuther, Pseudo-fermion functional renormalization group with magnetic fields, *Phys. Rev. B* **109**, 174414 (2024).
- [55] J. Oitmaa, C. Hamer, and W. Zheng, *Series Expansion Methods for Strongly Interacting Lattice Models* (Cambridge University Press, 2006).
- [56] J. Oitmaa, R. R. P. Singh, B. Javanparast, A. G. R. Day, B. V. Bagheri, and M. J. P. Gingras, Phase transition and thermal order-by-disorder in the pyrochlore antiferromagnet $\text{Er}_2\text{Ti}_2\text{O}_7$: A high-temperature series expansion study, *Phys. Rev. B* **88**, 220404 (2013).